

Current Biology

A neural population selective for song in human auditory cortex

Highlights

- Neural population responsive to singing, but not instrumental music or speech
- New statistical method infers neural populations from human intracranial responses
- fMRI used to map the spatial distribution of intracranial responses
- Intracranial responses replicate distinct music- and speech-selective populations

Authors

Sam V. Norman-Haignere, Jenelle Feather, Dana Boebinger, ..., Josh H. McDermott, Gerwin Schalk, Nancy Kanwisher

Correspondence

samuel_norman-haignere@urmc.rochester.edu

In brief

Using human intracranial recordings, Norman-Haignere et al. reveal a neural population that responds to singing, but not instrumental music or speech. This neural population was uncovered by modeling electrode responses as a weighted sum of canonical response components. The spatial distribution of each intracranial component was mapped using fMRI.

Article

A neural population selective for song in human auditory cortex

Sam V. Norman-Haignere,^{1,2,3,4,5,6,7,15,20,*} Jenelle Feather,^{7,8,9,16} Dana Boebinger,^{7,8,10,17} Peter Brunner,^{11,12,13} Anthony Ritaccio,^{11,14} Josh H. McDermott,^{7,8,9,10,18} Gerwin Schalk,¹¹ and Nancy Kanwisher^{7,8,9,19}

¹Zuckerman Institute, Columbia University, New York, NY, USA

²HHMI Fellow of the Life Sciences Research Foundation, Chevy Chase, MD, USA

³Laboratoire des Systèmes Perceptifs, Département d'Études Cognitives, ENS, PSL University, CNRS, Paris, France

⁴Department of Biostatistics & Computational Biology, University of Rochester Medical Center, Rochester, NY, USA

⁵Department of Neuroscience, University of Rochester Medical Center, Rochester, NY, USA

⁶Department of Biomedical Engineering, University of Rochester, Rochester, NY, USA

⁷Department of Brain and Cognitive Sciences, Massachusetts Institute of Technology, Cambridge, MA, USA

⁸McGovern Institute for Brain Research, Massachusetts Institute of Technology, Cambridge, MA, USA

⁹Center for Brains, Minds and Machines, Cambridge, MA, USA

¹⁰Program in Speech and Hearing Biosciences and Technology, Harvard University, Cambridge, MA, USA

¹¹Department of Neurology, Albany Medical College, Albany, NY, USA

¹²National Center for Adaptive Neurotechnologies, Albany, NY, USA

¹³Department of Neurosurgery, Washington University School of Medicine, St. Louis, MO, USA

¹⁴Department of Neurology, Mayo Clinic, Jacksonville, FL, USA

¹⁵Twitter: @SamNormanH

¹⁶Twitter: @jenellefeather

¹⁷Twitter: @dlboebinger

¹⁸Twitter: @JoshHMcDermott

¹⁹Twitter: @Nancy_Kanwisher

²⁰Lead contact

*Correspondence: samuel_norman-haignere@urmc.rochester.edu

<https://doi.org/10.1016/j.cub.2022.01.069>

SUMMARY

How is music represented in the brain? While neuroimaging has revealed some spatial segregation between responses to music versus other sounds, little is known about the neural code for music itself. To address this question, we developed a method to infer canonical response components of human auditory cortex using intracranial responses to natural sounds, and further used the superior coverage of fMRI to map their spatial distribution. The inferred components replicated many prior findings, including distinct neural selectivity for speech and music, but also revealed a novel component that responded nearly exclusively to music with singing. Song selectivity was not explainable by standard acoustic features, was located near speech- and music-selective responses, and was also evident in individual electrodes. These results suggest that representations of music are fractionated into subpopulations selective for different types of music, one of which is specialized for the analysis of song.

INTRODUCTION

Music is a quintessentially human capacity: it is present in some form in nearly every society^{1,2} and differs substantially from its closest analogs in non-human animals.³ Researchers have long debated whether the human brain has mechanisms dedicated to music, and if so, what computations those mechanisms perform.⁴ These questions have important implications for understanding the organization of auditory cortex,^{5,6} the neural basis of sensory deficits such as amusia,^{7,8} the consequences of auditory expertise,⁹ and the computational underpinnings of auditory behavior.¹⁰

Neuroimaging studies have suggested that representations of music diverge from those of other sound categories in human non-primary auditory cortex. Prior studies have observed non-

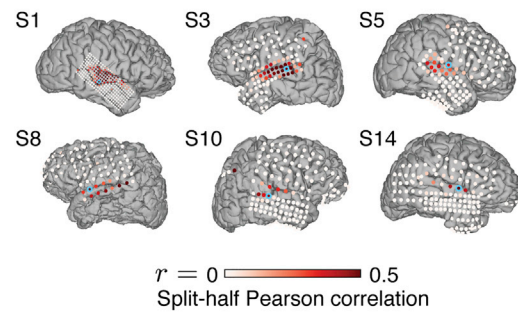
primary voxels with partial selectivity for music compared with other categories,^{5,11} and recent studies from our lab, which modeled fMRI voxels as weighted sums of multiple response components, inferred a component with clear music selectivity^{6,12} that was distinct from nearby speech-selective responses. However, little is known about how neural responses are organized within the domain of music, such as whether distinct subpopulations exist that are selective for particular types or features of music.¹³

Here, we examined the neural representation of music, and of natural sounds more broadly, using intracranial recordings from the human brain (ECoG, or electrocorticography), which have substantially better spatiotemporal resolution than non-invasive neuroimaging methods. We measured ECoG responses to a diverse set of 165 natural sounds (Figure 1A) and developed a

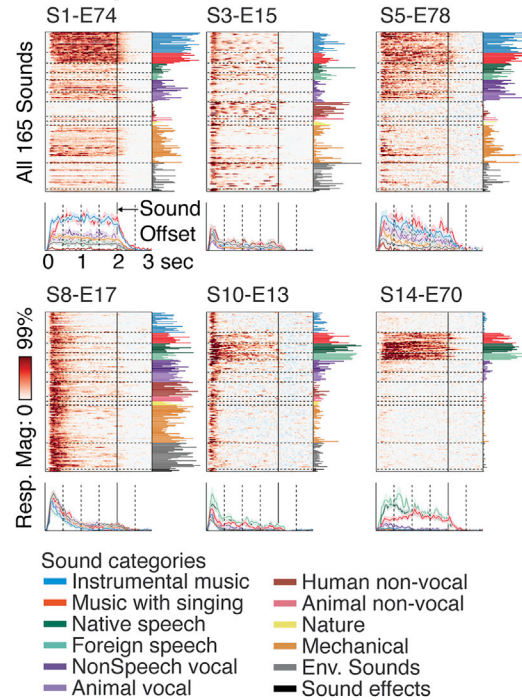
A 165 natural sounds

- | | | |
|-----------------------|---------------------|-------------------------|
| 1. Man speaking | 11. Running water | 21. Cellphone vibrating |
| 2. Flushing toilet | 12. Breathing | 22. Water dripping |
| 3. Pouring liquid | 13. Keys jangling | 23. Scratching |
| 4. Tooth-brushing | 14. Dishes clanking | 24. Car windows |
| 5. Woman speaking | 15. Ringtone | 25. Telephone ringing |
| 6. Car accelerating | 16. Microwave | 26. Chopping food |
| 7. Biting and chewing | 17. Dog barking | 27. Telephone dialing |
| 8. Laughing | 18. Walking | 28. Girl speaking |
| 9. Typing | 19. Road traffic | 29. Car horn |
| 10. Car engine | 20. Zipper | ... |

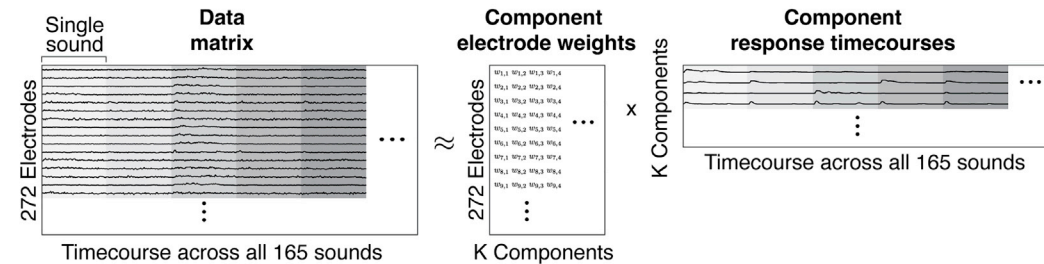
B Reliability of ECoG broadband gamma response to natural sounds



C Example electrodes



D Electrode decomposition



E Prediction accuracy vs. number of components

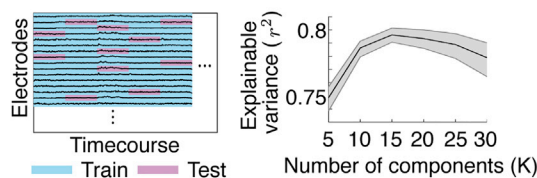


Figure 1. Overview of experiment and decomposition method

(A) The sound set consisted of 165 commonly heard sounds (each 2 s).⁶

(B) Electrodes were selected based on the split-half reliability of their broadband gamma response time course (70–140 Hz) to natural sounds (correlation between odd versus even repetitions). This panel plots reliability maps for six example subjects (of 15 total), illustrating the sparse and variable coverage. Subjects were numbered based on the number of reliable electrodes in their dataset. Blue circles outline the example electrodes shown in (C).

(C) The broadband gamma response time course of several example electrodes to all 165 sounds, plotted as a raster. The time-averaged response to each sound is plotted to the right of the raster. The sounds have been grouped and colored based on membership in one of 12 sound categories. Below each raster, we plot the average response time course to each category with greater than 5 exemplars. Error bars plot the median and central 68% of the sampling distribution (equivalent to one standard error for a Gaussian), computed via bootstrapping across sounds.

(D) Electrode time courses were compiled in a matrix, where each row contains the full response time course of each electrode (from 0 to 3 s post-stimulus onset), concatenated across all 165 sounds tested. The data matrix was approximated as the product of a response time course matrix, which contains a small number of canonical response time courses that are shared across all electrodes, with an electrode weight matrix that expresses the contribution of each component time course to each electrode (see [Figures S1](#) and [S7](#) and the [STAR Methods](#) for additional modeling details).

(E) Cross-validation was used to compare models ([Figure S1G](#)) and determine the number of components. The data matrix was divided into cells, with one cell containing the response time course of a single electrode to a single sound. The model was trained on a randomly chosen subset of 80% of cells and

(legend continued on next page)

component decomposition algorithm adapted to the statistical structure of ECoG responses. To overcome the sparse and restricted coverage of ECoG recordings, we estimated the spatial distribution of each component using a large dataset of fMRI responses to the same sounds (comprised of 88 2-h scans from 30 subjects across two studies^{6,12}).

The components revealed by this analysis replicated many prior findings including tonotopic frequency selectivity,^{14–17} spectrotemporal modulation tuning,^{18–20} spatially organized onset responses,²¹ as well as selectivity for speech, music, and vocalizations.^{5,6,11,22,23} Our key novel finding is that one of these components responded nearly exclusively to music with singing. This finding indicates that the human brain contains a neural population specific to the analysis of song.

RESULTS

Intracranial recordings

We measured ECoG responses to a diverse set of 165 natural sounds, designed to include many commonly heard and recognizable sounds from daily life (Figure 1A).⁶ We identified a set of 272 electrodes across 15 patients with a reliable broadband gamma response to the sound set (split-half correlation >0.2; Figure 1B). The number of reliable electrodes varied substantially across subjects due to the sparse, clinically driven coverage (Figure 1B). Individual electrodes showed diverse responses, including strong responses at sound onset and selective responses to speech (Figure 1C).

Electrode decomposition

Rather than analyze individual electrodes, we attempted to explain the response of all 272 electrodes as the weighted sum of a small number of canonical response time courses. Each component time course could potentially reflect a different neuronal population in auditory cortex with its weights reflecting the contribution of that population to each electrode.

To identify components, we represented the electrode responses as a matrix, in which each row contained the concatenated response time courses of a single electrode to all 165 sounds (Figure 1D). We used matrix factorization to approximate this matrix as the product of a component response time course matrix and a component electrode weight matrix. In general, matrix factorization is ill-posed and needs to be constrained by statistical criteria. We identified three statistical properties of auditory broadband gamma that could be used as constraints (Figures S1A–S1D): (1) relative to silence, sound-driven responses are nearly always excitatory; (2) responses are sparse across both time/stimuli and electrodes; and (3) responses are temporally smooth and the extent of this smoothness varies across electrodes.

We designed a component model that captured these statistical properties (Figure S1E). The model approximates each electrode's response time course ($\mathbf{e}_i(t)$) as the weighted sum of K component response time courses ($\mathbf{r}_k(t)$):

$$\mathbf{e}_i(t) \approx \sum_{k=1}^K w_{ik} \mathbf{r}_k(t). \quad (\text{Equation 1})$$

The component responses and weights were constrained to be non-negative, ensuring excitatory responses. To capture sparsity and smoothness, we modeled the response time course of each component as the convolution of sparse activations ($\mathbf{a}_k(t)$) with a smoothing kernel ($\mathbf{h}_k(t)$), learned separately for each component:

$$\mathbf{r}_k(t) = \mathbf{a}_k(t) * \mathbf{h}_k(t). \quad (\text{Equation 2})$$

Sparsity was imposed by a standard L1 penalty. We focus on the results of this model because it yielded better cross-validated prediction accuracy than competing models (Figure S1G). However, our key results were evident using a simpler model that only imposed non-negativity on the responses and weights (non-negative matrix factorization, or NMF; Figure S2A).

We found that we could estimate ~ 15 components before overfitting the dataset (Figure 1E). We focus on a subset of 10 particularly reliable components that were present in the NMF model (Figure S2A), were stable across the number of components, and explained responses across multiple subjects (Figures S2B and S2C) (Figure S2D plots 5 less reliable components). Components were numbered based on the total magnitude of their responses and weights.

Speech and music-selective components

We first describe three components that responded selectively to speech or music (Figures 2A and 2B). We emphasize that the sound category labels played no role in the decomposition algorithm. For each component, we plot its response (Figure 2A) as well as an anatomical map of its electrode weights (Figure 2B).

Because ECoG coverage is highly restricted, we complemented the electrode weight map with a second map, computed using a dataset of fMRI responses to the same sound set across a non-overlapping set of 30 subjects.^{6,12} We computed this map by regressing the time-averaged response of the ECoG components (each a 165-dimensional vector) against the time-averaged response of each fMRI voxel (the fMRI response is too coarse to resolve within-sound temporal variation). The regression weights were then averaged across subjects to form a group map. This approach enabled us to leverage the dense and comprehensive coverage of fMRI to provide an estimate of the full weight-map for each ECoG-derived component.

We correlated the fMRI and ECoG maps and compared these correlation values with the cross-subject reliability of each modality (electrode weights were resampled to standard anatomical coordinates using a 5 mm FWHM smoothing kernel, so that they could be correlated with the fMRI weight maps) (Figure 2C). As expected, the fMRI maps had much higher cross-subject reliability, due to superior coverage and more subjects. The

was then tested on the remaining 20% of cells. This panel plots the squared test correlation between measured and predicted responses for different numbers of components (averaged across all electrodes). The correlation has been noise-corrected using the test-retest reliability of the electrode responses so as to provide an estimate of explainable variance. Error bars plot the median and central 68% of the sampling distribution, computed via bootstrapping across subjects.

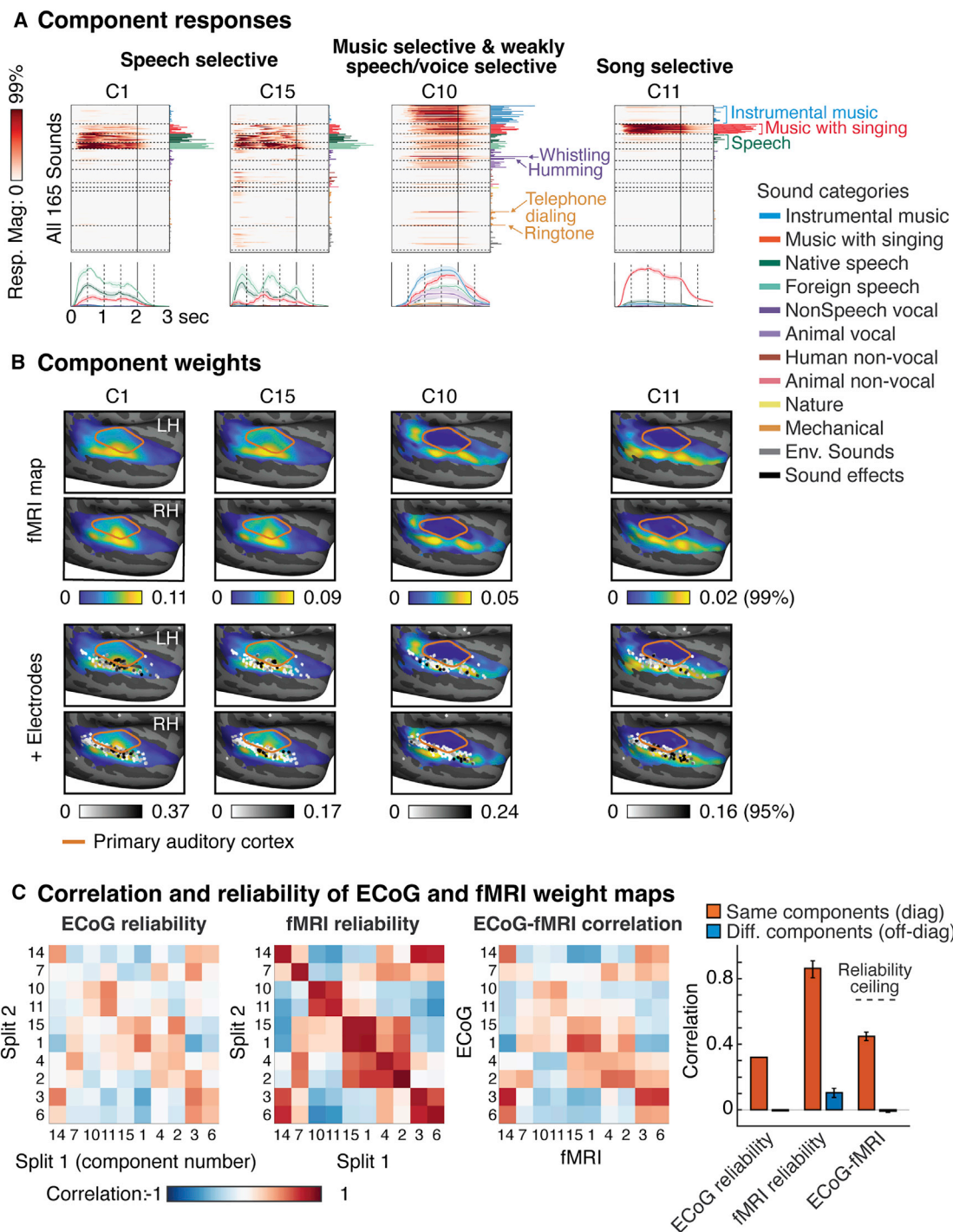


Figure 2. Category-selective components

(A) The response time course of four components that responded selectively to speech or music sounds. The format is the same as the example electrodes shown in Figure 1C. Figure S2A plots component responses from a simpler NMF model. Figure S3 shows additional acoustic analyses of the speech-selective components.

(B) The anatomical distribution of weights for each component. We used fMRI responses to the same sounds from 30 non-overlapping subjects to get a second estimate of each component's anatomical distribution (top panel). The fMRI weights were computed by regressing the time-averaged response of the ECoG-derived components against the response of each fMRI voxel. The bottom panel overlays the electrode weights computed directly from the ECoG data (each circle corresponding to one electrode). The orange outlines show the approximate location of primary auditory cortex, defined tonotopically in our prior fMRI study.⁶ The weight scale is arbitrary. The upper limit of the color scale was set to 99% (fMRI) or 95% (ECoG) of the weight distribution for each component (a

(legend continued on next page)

correlation between fMRI and ECoG maps for corresponding components was slightly higher than the reliability of the ECoG maps themselves and much higher than that for mismatching components ($p < 0.001$ via bootstrapping across the fMRI subjects). These findings suggest a close correspondence between the fMRI and ECoG maps that is primarily limited by the sparse coverage of ECoG recordings and thus demonstrates the utility of combining the precision of ECoG recordings with the spatial coverage of fMRI. We primarily used the fMRI maps to test for laterality effects, due to its dense bilateral coverage across many subjects.

Two components (C1 and C15) responded nearly exclusively to speech, with virtually no response to all other sounds including non-speech vocalizations. These components responded similarly to native and foreign speech sounds (all subjects were native English speakers), consistent with prior work showing that speech selectivity in STG is not driven by linguistic meaning.^{6,23} C1 and C15 responded at different time points within each speech utterance. Some of this response pattern to speech could be predicted by a linear spectrotemporal receptive field (STRF) ($p < 0.01$; see STAR Methods for details) with C15 showing a higher frequency STRF compared with C1 (Figures S3A and S3B). However, the overall predictions of a STRF model across the full sound set were poor and failed to capture these components' selectivity for speech (Figure S3C). These results suggest that C1 and C15 are nonlinearly tuned for distinct speech-specific features or classes that happen to have distinct frequency spectra (e.g., low-frequency voiced phonemes versus high-frequency fricatives).^{24–27}

The weights for the speech-selective components were primarily clustered in middle STG, with no significant difference between the two hemispheres ($p > 0.73$ uncorrected for the number of components; via bootstrapping across subjects), consistent with prior studies.^{5,12,23} The time-averaged response of C1 and C15 was very similar, which limited our ability to anatomically distinguish these two components with fMRI.

One component (C10) responded strongly to both instrumental music and music with singing (average[instrumental music, sung music] > average[all non-music categories]: $p < 0.001$ via bootstrapping, Bonferroni-corrected for the number of components) and produced an intermediate response to speech and other human vocalizations. The intermediate response to speech/voice could reflect imperfect disentangling of speech and music selectivity by our component model, potentially due to limited coverage of the superior temporal plane where music selectivity is prominent and speech selectivity is weak. C10 also showed the longest response latency of all the inferred components (708 ms),

suggesting a longer integration window²⁸ (latencies were defined as the time needed for the response to reach half its maximum). The weights for C10 showed three hotspots in posterior, middle, and anterior STG, with no difference between the two hemispheres ($p = 0.63$ uncorrected). This anatomical profile is similar to the music-selective component we previously inferred using just fMRI data,^{6,12} but the cluster in middle STG was more prominent here likely due to stronger speech responses. These results replicate our prior fMRI findings, showing distinct clusters of speech and music selectivity in non-primary auditory cortex.

Song selectivity

Our key novel finding is that one component (C11) responded nearly exclusively to sung music: every music stimulus with singing produced a high response whereas all other sounds, including both speech and instrumental music, produced little to no response (sung music always had instrumental backing). Because our component model approximates electrodes as weighted sums of multiple components, the model should not have needed a separate song-selective component if song selectivity simply reflected a sum of speech and music selectivity. The component response confirmed this expectation: the response to sung music was substantially and significantly higher than the sum of the response to speech and instrumental music (sung music > max[English speech, foreign speech] + instrumental music: $p < 0.001$ via bootstrapping, Bonferroni-corrected). Moreover, the response of C11 could not be explained as a linear combination of our previously reported fMRI components that showed clear selectivity for music and speech individually (Figures S4A and S4B). C11 had a relatively long latency (298 ms), and its weights were concentrated in non-primary auditory cortex, nearby to both speech- and music-selective responses in middle and anterior STG, respectively. C11 was not significantly lateralized in the fMRI weight map ($p = 0.48$ uncorrected), and although the electrode weights appear somewhat right lateralized, this difference was also not significant ($p = 0.09$ uncorrected), though we note that laterality comparisons with ECoG data are generally underpowered.

Hypothesis-driven component analysis

Are statistical assumptions like non-negativity and sparsity necessary to detect speech, music, and song selectivity? To answer this question, we performed a simpler analysis, where we attempted to learn a weighted sum of electrode responses that approximated a binary preference for speech, music, or singing (via regularized regression), using cross-validation across sounds to prevent overfitting. This analysis successfully

higher threshold for fMRI because of its greater coverage). The lower limit was set to 0 (ECoG weights were constrained to be non-negative, and the fMRI weights were in practice mostly positive). Figures S2B and S2C show how the electrode weights are distributed across subjects.

(C) This panel quantifies the similarity of the fMRI and ECoG weight maps relative to the maximum possible similarity given the across-subject reliability of each modality. The leftmost two matrices show the correlation between all pairs of component weight maps, measured using two non-overlapping sets of subjects from the same modality (left matrix, ECoG; middle, fMRI). The right matrix plots the correlation between ECoG and fMRI weight maps. The bar plots at right show the average correlation for corresponding (matrix diagonal) and non-corresponding components (off-diagonal). If the modalities are consistent, the correlation should be higher for corresponding components. The dashed line shows an estimate of the maximum possible correlation between ECoG and fMRI maps given the reliability of the two modalities. All 10 reliable components are shown, including those without strong category selectivity (see Figure 5). The components were arranged by the similarity of their response profiles since components with more similar response profiles also tended to have more similar anatomical distributions. ECoG electrode weights were resampled to standard anatomical coordinates (using a 5-mm FWHM smoothing kernel) so that they could be compared across subjects and with the fMRI maps (smoothed with a 5-mm FWHM kernel). Error bars show the central 68% of the sampling distribution, computed by bootstrapping across fMRI subjects. Bootstrapping across ECoG subjects was not feasible because of variable coverage.

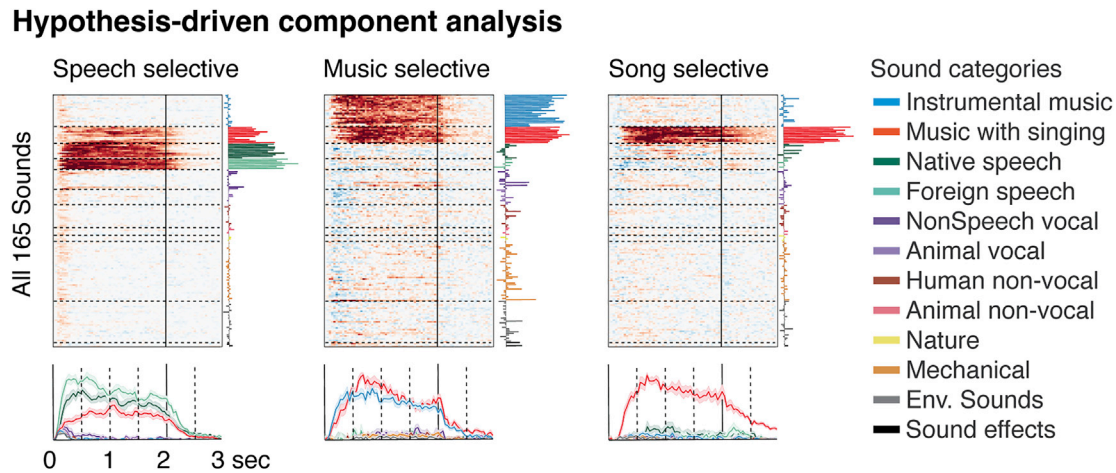


Figure 3. Hypothesis-driven component analysis

In contrast to our data-driven decomposition, here we used category labels to explicitly search for components that showed selectivity for speech, music, or song. Specifically, we attempted to learn a weighted sum of the electrodes (via regularized regression) that came as close as possible to a binary response to speech (English or Foreign speech), music (instrumental or sung music), or sung music. Cross-validation across sounds was used to prevent overfitting. Sung music was excluded when estimating the electrode weights for the speech-selective component, since it contains an intermediate amount of speech. Format is the same as Figure 2A.

identified components with a nearly binary response preference for speech, music, and song (Figure 3). Since binary song selectivity cannot be produced by a weighted sum of speech and music selectivity, this result provides further evidence for a nonlinear response to song. The music-selective component obtained from this hypothesis-driven analysis showed no response to speech and voice sounds, suggesting that music selectivity is indeed distinct from speech/voice selectivity, even though our data-driven analysis was not able to perfectly disentangle music selectivity from speech/voice selectivity using purely statistical criteria.

Selectivity for spectrotemporal modulation statistics

Can speech, music, and song selectivity be explained by generic acoustic representations, such as spectrotemporal modulations?^{18–20} To answer this question, we measured ECoG responses in a subset of 10 patients to a new set of 36 natural sounds as well as corresponding set of 36 synthetic sounds, each of which was synthesized to have similar spectrotemporal modulation statistics as one of the natural sounds (Figure 4A).²⁹ Because the synthetic sounds are only constrained in their spectrotemporal modulation statistics they lack higher-order structure important to speech and music (e.g., syllabic or harmonic structure). Of the 36 natural sounds, there were 8 speech and 10 music stimuli, two of which contained singing.

We estimated the response of each component from the 165-sound experiment to this new sound set, providing an independent validation of the components' selectivity (Figures 4B and 4C). Specifically, we fixed the component electrode weights to those estimated from the 165-sound experiment, and we estimated a new set of component response time courses that best approximated the electrode responses from the modulation-matching experiment. All of the category-selective components replicated their selectivity for natural speech, music, or singing and produced substantially weaker responses to modulation-

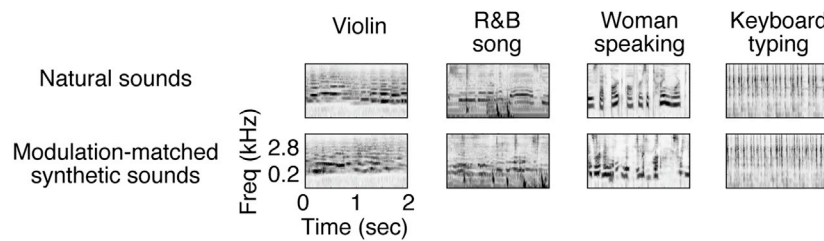
matched synthetic sounds ($p < 0.01$ via a sign test comparing natural and modulation-matched sounds from the preferred category of each component; see STAR Methods for details). The song-selective component (C11) responded nearly exclusively to the natural sung music with almost no response to natural speech, natural instrumental music, and modulation-matched sung music. These findings demonstrate that speech, music, and song selectivity cannot be explained by standard frequency and modulation statistics.

Components selective for standard acoustic features

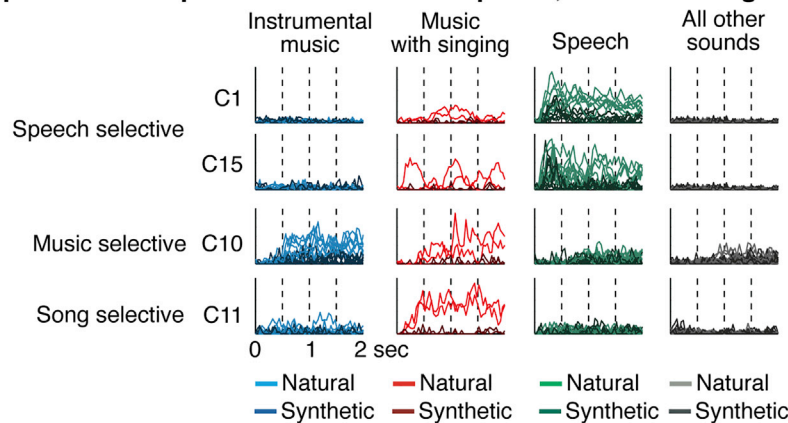
Six reliable ECoG components exhibited weaker category selectivity and showed evidence of selectivity for standard acoustic features (Figure 5). These components had weights that clustered in and around primary auditory cortex (Figure 5B) and had relatively fast latencies (71–124 ms, apart from C14, which responded at sound offset). Responses to natural and modulation-matched synthetic sounds were more similar than those for the category-selective components (Figure 5C), suggesting that frequency and modulation statistics account for more of their response. Most of the response variance in these components could be explained by a strong response at sound onset or offset, the magnitude of which varied across the sound set. We captured this variation using the first principal component (PC) of the sound \times time matrix, which explained the majority of the response variance (>58% in all 6 components). The first PC approximates the sound \times time response matrix using a single time course, the magnitude of which varies across the sound set. We correlated this cross-sound variation with acoustic measures of audio frequency (Figure 5D) and spectrotemporal modulation energy (Figure 5E).

C3 responded strongly at sound onset for nearly all sounds and had weights that clustered in posterior auditory cortex, replicating prior findings.²¹ C14 responded strongly at sound offset, and also had weights clustered in posterior auditory cortex,

A Cochleagrams of example natural and modulation-matched synthetic sounds



B Response of components selective for speech, music or song



C Time-averaged response

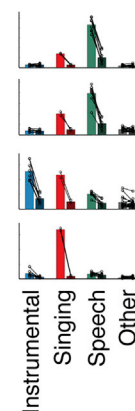


Figure 4. Component responses to natural and modulation-matched synthetic sounds

(A) Cochleagrams of example natural sounds and corresponding synthetic sounds with matched spectrotemporal modulation statistics.²⁹ Cochleagrams plot energy as a function of time and frequency, similar to a spectrogram, but measured from filters designed to mimic cochlear frequency tuning (stimuli lasted 4 s, but to facilitate inspection, only the first 2 s of each cochleagram is plotted). The natural sounds tested in the modulation-matching experiment were distinct from 165 natural sounds used to identify components.

(B) The response of the speech, music, and song-selective components to natural and modulation-matched sounds. The sounds have been grouped into four categories: instrumental music (blue), music with singing (red), speech (green, both English and foreign), and all other sounds (black/gray). Each line shows the response time course (first 2 s) to a single natural sound (lighter colors) or modulation-matched synthetic sound (darker colors).

(C) The time-averaged component response to each pair of natural and modulation-matched sounds (lines connect pairs), along with the mean grand response across all natural (lighter bars) and modulation-matched (darker bars) sounds from each category.

which to the best of our knowledge is the first demonstration of an anatomically organized offset response in human auditory cortex. C2 and C6 partially reflected tonotopic organization:^{14–17} their response correlated with measures of low and high-frequency energy, respectively, and their weights clustered in corresponding low- and high-frequency regions of primary auditory cortex. C7 replicated prior findings of “pitch” or “tone” selectivity:^{30–32} its response correlated with spectrotemporal modulation energy at fine spectral scales and slow temporal rates, which is characteristic of tonal sounds, and its anatomy overlapped both low-frequency regions of primary auditory cortex and more anterior non-primary regions. Finally, C4 responded preferentially to vocal sounds including non-speech vocalizations, consistent with prior studies,²² and was the only component that showed significant right lateralization ($p < 0.05$ after Bonferroni correction for multiple components).³³ Both C4 and C7 showed modest selectivity for natural versus modulation-matched sounds and had anatomical weights that straddled primary/non-primary auditory cortex, suggesting both lower- and higher-order selectivity.

Finally, we measured the overall fraction of the across-sound response variance predictable by standard acoustic features, category labels, or their combination (Figure S5A). Category labels predicted more variance than standard acoustic features in the components selective for speech, music, and song ($p < 0.01$ for C1, C15, and C11; $p = 0.10$ for C10; computed via bootstrapping across sounds), and acoustic features added little additional variance. Standard acoustic features were especially poor predictors of song selectivity (Figure S5B). By contrast, standard acoustic features predicted more variance than category labels in the more primary-like components ($p < 0.01$ for C4, C6, and C7; $p < 0.05$ for C3; $p = 0.53$ for C2; $p = 0.44$ for C14) (Figure S5A).

We note that the total amount of variance predicted by the acoustic features was relatively high in some category-selective components (e.g., $r^2 > 0.59$ in the speech-selective components C1 and C15). However, these acoustic features explained little additional variance above and beyond that explained by category labels, and the response to modulation-matched synthetic sounds was weak in these components (Figure 4), despite being

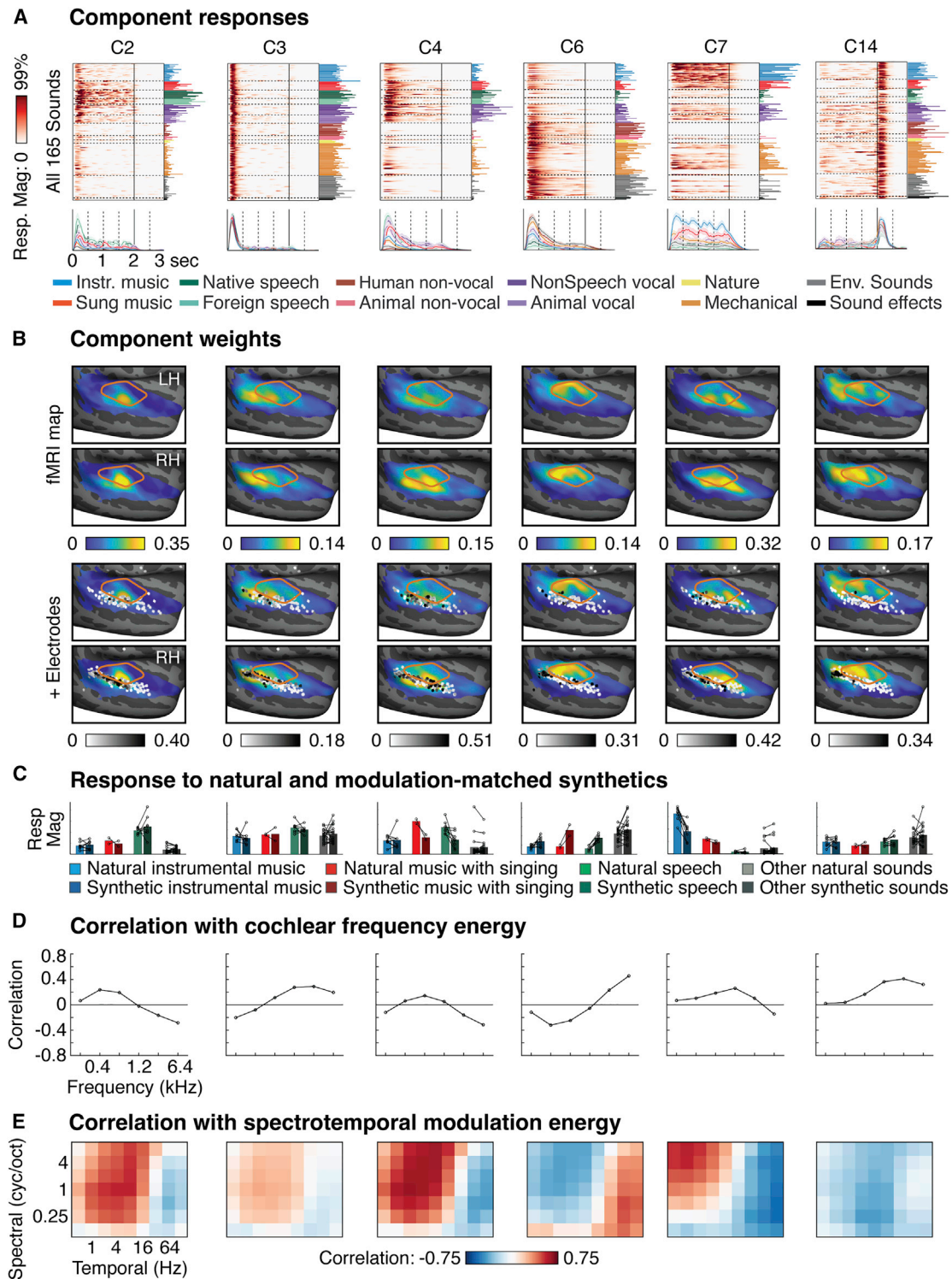


Figure 5. Components selective for standard acoustic features

(A and B) Responses and anatomical distributions for 6 components whose responses suggested selectivity for standard acoustic features (see [Figure S2D](#) for responses from other less reliable components). Same format as [Figures 2A](#) and [2B](#).

(C) Component responses to natural and modulation-matched synthetic sounds. Same format as [Figure 4C](#).

(D and E) Correlations between component responses and measures of audio frequency (D) and spectrotemporal modulation energy (E), computed from a cochleagram representation of sound. See text for details. [Figure S5](#) shows the overall prediction accuracy of standard acoustic features and category labels in each component.

matched on the same features used to compute the predictions. Thus, these seemingly good predictions may be driven by spurious correlations across natural sounds between standard acoustic features and higher-order, category-specific features (e.g., phonemic structure).³⁴ Our synthesis approach addresses this problem because the synthetic sounds are only constrained by frequency and modulation features, effectively decoupling them from higher-order features of sound.²⁹

Single-electrode analyses

We tested whether we could also observe speech, music, and song selectivity in individual electrodes without any component modeling. Based on prior studies, we expected that speech selectivity would be prominent in individual electrodes, but it was unclear if music or song selectivity would be robustly present, given that music selectivity is weak in individual fMRI voxels.^{6,12} We identified electrodes selective for speech, music, or song using a subset of data and then measured their response in left-out, independent data. Electrode identification involved three steps. First, we measured the average response across time and stimuli to all sound categories with more than five exemplars. Second, we identified a pool of electrodes with a highly selective (selectivity > 0.6) and significant ($p < 0.001$ via bootstrapping) response to either speech, music, or song compared with all other categories. Selectivity was measured by contrasting the maximum response across all speech and music categories (English speech, foreign speech, sung music, instrumental music) with the maximum response across all other non-music and non-speech categories (we used the selectivity index $[A - B]/A$, where A and B are the categories being contrasted; the $[A - B]$ contrast was bootstrapped and compared against 0 to assess significance). Third, from this pool of electrodes, we formed three groups: those that responded significantly more to speech than all else ($\max[\text{English speech, foreign speech}] > \max[\text{non-speech categories except sung music}]$), music than all else ($\text{instrumental music} > \max[\text{non-music categories}]$), or that exhibited super-additive selectivity for singing ($\text{sung music} > \max[\text{English speech, foreign speech}] + \text{instrumental music}$) (using a threshold of $p < 0.01$, via bootstrapping).

We show the top electrodes most significantly responsive to speech, music, or singing as well as the average response across all electrodes from each group (Figure 6). As expected, we observed many speech-selective electrodes (173 electrodes across 14 subjects). Notably, we also observed a small number of music and song-selective electrodes (11 music-selective electrodes across 4 subjects, and 7 song-selective electrodes across 3 subjects). Despite their small number, each music- and song-selective electrode replicated their selectivity for music or song in independent data ($p < 0.05$ via bootstrapping for every electrode individually; $p < 0.001$ for responses averaged across all music and song-selective electrodes; selectivity was measured using the same contrasts described above). Moreover, modulation-matched synthetic sounds produced much weaker responses than natural sounds from the preferred category in these electrodes ($p < 0.01$ via a sign test between responses to natural and model-matched sounds, applied to the average response of speech, music, and song-selective electrodes). The three subjects (S1, S3, and S4) with song-selective electrodes had more sound-responsive electrodes than all but

one other subject (S2; subjects were ordered based on the number of sound-responsive electrodes they showed) and did not have unusually high levels of musical training (S1 reported no musical training, and S3 and S4 both reported 4 years of music classes in elementary/middle school). Thus, it seems likely that these subjects showed song-selective electrodes simply because we had better coverage of their auditory cortex.

The presence of song selectivity in individual electrodes demonstrates that our component analysis did not infer a form of selectivity that is not present in the data. At the same time, only a handful of electrodes showed song selectivity, and the selectivity of these electrodes was substantially weaker than the song-selective component we identified using purely statistical criteria ($p < 0.001$ via bootstrap, using the super-additive song selectivity metric). This observation suggests that our component method isolated selectivity for singing by de-mixing weak song selectivity present in individual electrodes. To test this hypothesis, we re-ran both our data-driven (Figure 2) and hypothesis-driven (Figure 3) component analyses after discarding all song-selective electrodes. These analyses revealed a nearly identical song-selective component (Figure S6A). This finding demonstrates that we can infer song selectivity using two non-overlapping sets of electrodes and two different analysis approaches.

The uneven distribution of electrodes across subjects made us wonder whether our findings were driven by individual subjects. The electrodes from just S1, for example, comprised ~25% of the dataset (70 of 272 electrodes). To address this question, we repeated our data-driven and hypothesis-driven component analyses 15 times, each time excluding all the electrodes from one subject. We observed a clear song-selective component in every case (the correlation between the response of the song-selective component derived from all subjects and those derived from reduced datasets was greater than 0.9 in all cases) (Figure S6B plots the song-selective components inferred when excluding data from S1). When we discarded all of the data from all three subjects with song-selective electrodes, thus discarding nearly half the dataset (122 of 272 electrodes), we still recovered a song-selective component using our hypothesis-driven method, but not using our data-driven method (Figure S6C). We note that detecting song selectivity using our hypothesis-driven approach is highly non-trivial: when we applied the same approach to a standard acoustic representation or to our previously inferred fMRI components, we did not recover a song-selective component (Figures S4A, S4B, and S5B). Thus, the failure of our data-driven method is not because song selectivity is absent, but instead reflects the inherent challenge of unmixing different response patterns using purely statistical criteria, particularly with a modestly sized dataset. Overall, these findings demonstrate that song selectivity is robustly present across multiple subjects.

Prediction of music and speech selectivity detected with fMRI

Why were we able to observe a song-selective component that was not evident in prior fMRI studies? One natural hypothesis is that ECoG is a finer-grained measure of neural activity and thus allowed us to resolve finer-grained selectivity. If this hypothesis were true, we might expect coarser fMRI response patterns to be predictable from finer-grained ECoG responses, but not vice versa. We have already shown that the song-selective ECoG

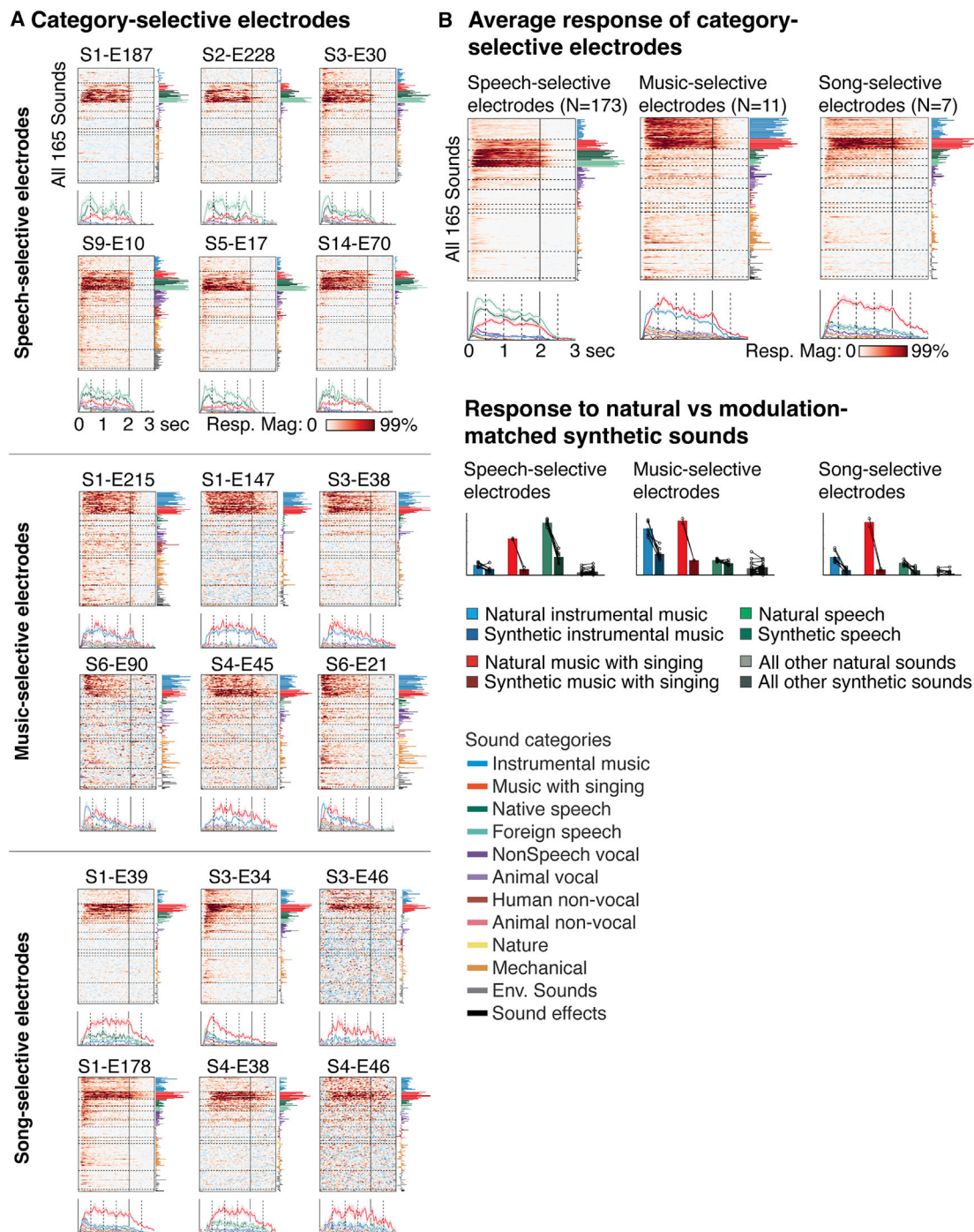


Figure 6. The response of individual electrodes selective for speech, music, or song

We selected speech- (top), music- (middle), and song-selective (bottom) electrodes and then measured their responses in independent data.

(A) The top six electrodes that showed the most significant response preference for each category in the subset of data used for electrode selection. For speech-selective electrodes, the top 6 electrodes came from 2 subjects (2 from S1 and 4 from S2), and therefore, we instead plot the top electrode from 6 different subjects to show the consistency/diversity across subjects. Same format as Figure 2A.

(B) The average response (in independent data) across all electrodes identified as speech, music, or song selective.

(C) The average response of speech-, music-, and song-selective electrodes to natural and modulation-matched synthetic sounds. Same format as Figure 4C. Figure S6 shows the effect of excluding song-selective electrodes, as well as individual subjects, on the inference of a song-selective component.

Prediction of speech- and music-selective fMRI components

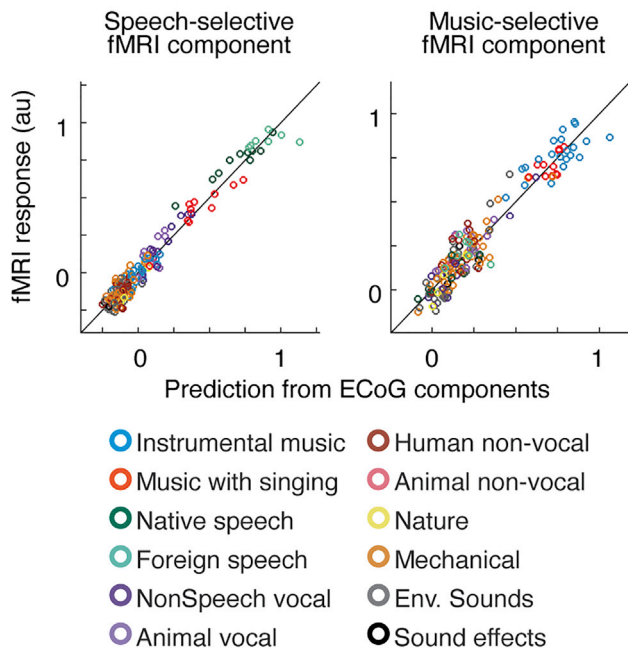


Figure 7. Prediction of speech and music selectivity detected with fMRI

We attempted to predict the response of the speech- and music-selective fMRI components inferred in our prior study⁶ as a weighted combination of the ECoG components identified here (using ridge regression, cross-validated across sounds). The ECoG component responses were time-averaged for this analysis. This figure plots the measured and predicted response of each component. Figure S4 shows the result of attempting to predict the ECoG song-selective component from fMRI components and voxels.

component cannot be predicted from our previously identified fMRI components (Figures S4A and S4B).^{6,12} Here, we ask the reverse question: whether the speech- and music-selective components detected in our fMRI study can be predicted from the time-averaged response of the ECoG components identified here (using cross-validated linear regression). We found that the ECoG predictions were surprisingly accurate, accounting for greater than 95% of the explainable response variance in both the speech- and music-selective fMRI components (Figure 7). This finding suggests that the ECoG components are indeed more fine-grained compared with those inferred using fMRI.

Weak song selectivity in fMRI voxels

While the fMRI components from our prior study showed no evidence of song selectivity (Figures S4A and S4B), these components do not explain all of the voxel response variance (~80%–90%), and it is possible that song selectivity might account for some of the residual variance. This question is relevant because we used the fMRI voxels to get a second estimate of each component's spatial distribution, which is only relevant for the song-selective component if the voxels contain some song selectivity. To address this question, we again attempted to predict the time-averaged response of the song-selective ECoG

component via cross-validated regression, but instead of using the fMRI components, we used the original voxel responses (using voxels from all 30 subjects, though results were often similar for individual subjects). We found that the voxel predictions showed weak but significant super-additive song selectivity in independent data (Figures S4C and S4D) ($p < 0.05$ via bootstrapping across sounds). The song selectivity of the voxel predictions was much weaker than that observed for the ECoG component ($p < 0.001$), but stronger than that observed for our fMRI components (Figures S4A and S4B; $p < 0.001$) and for standard acoustic features (Figure S5B; $p < 0.05$). Thus, fMRI voxels contain some song selectivity, but this selectivity is weak compared with ECoG.

DISCUSSION

Our study reveals that the human brain contains a neural population selective for song that is distinct from neural responses to music and speech. Song selectivity was demonstrated using (1) a statistical decomposition method that was blind to the properties of the stimuli; (2) a simpler, hypothesis-driven component method; and (3) responses from individual electrodes. Song selectivity was co-located with music- and speech-selective responses in the middle and anterior STG and could not be explained by standard frequency and modulation features. These findings suggest that music is represented by multiple distinct neural populations that are selective for different aspects of music, at least one of which responds specifically to singing. These findings were enabled by a novel decomposition method for inferring response components from ECoG data, and by the use of fMRI to provide a more reliable and comprehensive spatial map of each inferred component.

Implications of song selectivity

Although song stimuli have frequently been used to explore the neural basis of music and speech perception,^{35–38} to the best of our knowledge, our findings provide the first evidence for a neural population specifically involved in the perception of song.

What sound features underlie song selectivity? Singing is distinguished from speech by its melodic intonation contour and rhythmicity³⁹ and from instrumental music by vocal resonances and other voice-specific structure.⁴⁰ Thus, a natural hypothesis is that song-selective neural populations nonlinearly integrate across multiple features³⁸ that differentiate singing from speech and music,³⁶ such as melodic intonation and vocal resonances. Given the location and long latency of the song-selective component, this integration is likely performed by non-primary neural populations that get input from neural populations in primary auditory cortex with shorter latencies.

Why are song-selective responses anatomically situated between speech- and music-selective responses? The location of category-selective regions may in part reflect biases in the low-level properties of these categories, coupled with coarse-scale maps (e.g., tonotopy) that are present early in development.^{41–43} However, multiple lines of evidence (Figures 4 and S5) suggest that this type of frequency and modulation tuning only explains a small fraction of category-selective responses. Recent studies have demonstrated that deep neural networks can replicate category-selective anatomical organization in high-level visual cortex when imbued with a notion of spatial

topography and a simple wiring constraint,^{44,45} providing a functional hypothesis for why this organization emerges. Speech- and music-trained DNNs have shown promise in predicting non-primary auditory cortical responses,¹⁰ and future research could test whether these networks can explain the functional and anatomical organization uncovered here.

How do song-selective populations interact with regions beyond auditory cortex? There are reports of responses to singing and other types of music in motor/premotor regions,^{46–48} which could in principle influence responses in auditory cortex through feedback, and there is broad consensus that auditory circuits play a critical role in the production of speech and other vocal sounds such as singing.^{48–51} Listening to singing can induce strong emotions⁵² and memories⁵³ that plausibly depend upon interactions between song-selective neural populations and regions of the medial temporal lobe and basal forebrain.^{54,55} Our study opens the door to studying such interactions with greater precision, for example, by stimulating auditory electrodes that project strongly on music- or song-selective components and measuring the impact on downstream regions, as well as any concomitant changes in patients' subjective perception.^{56,57}

How might song selectivity have arisen in the first place? The visual word form area demonstrates that category-selective neural populations can arise purely from experience, since reading is a recent cultural invention.⁵⁸ Music could similarly arise from individual experience, particularly since it engages reward-related circuits in the basal forebrain,^{54,55} whose activity can induce long-term plasticity in the auditory cortex.⁵⁹ However, unlike reading, singing could plausibly have shaped neural circuits over the course of evolution,⁶⁰ since it appears to be a natural and instinctive behavior that is widely present across human societies² and does not require technology. Indeed, we observed music- and song-selective electrodes in a subject with no reported musical training (S1), consistent with a recent finding from our lab that music selectivity does not depend on explicit training.¹² On the other hand, almost all listeners have extensive implicit knowledge of music and song gained through listening over the lifetime.^{61,62} Thus, many questions remain about the origins of song and music selectivity in auditory cortex.

What are the perceptual consequences of neural song selectivity? Vocal melodies are better remembered than instrumental melodies,⁵³ which may reflect greater salience for sung compared with instrumental music.⁶³ The neural basis of this increased salience remains unclear, but one possibility is that more salient stimuli might have more distinctive representations in high-level sensory regions.⁶⁴ We hope our study will catalyze research that focuses specifically on the perception of song, distinct from music and speech perception more generally.

Music selectivity

Our findings validate our prior fMRI studies, which reported a music-selective component with substantially greater selectivity than that present in individual voxels,^{6,12} which we hypothesized was due to the overlap of neural populations within voxels. Consistent with this hypothesis, some of the electrodes that showed the strongest music selectivity (e.g., S1-E147, S1-E215) were sampled by a high-density grid with particularly small electrodes (1-mm exposed diameter), suggesting that high spatial resolution is indeed important for detecting music selectivity in individual electrodes.

Voice and speech selectivity

Prior studies have identified a large region within the STG that responds preferentially to non-speech voice sounds (the “temporal voice area”).⁶⁵ However, the extent to which speech- and voice-selective responses are distinct in the brain has remained unclear: speech-selective responses typically show above baseline responses to non-speech vocalizations,⁶ and the temporal voice area responds more strongly to speech than other non-speech vocalizations.⁶⁵ By contrast, the speech-selective components (C1, C15) identified in this study showed virtually no response to non-speech vocalizations, and C4 responded strongly to a wide range of speech and non-speech vocalizations. This finding suggests that speech and voice indeed have spatially distinct representations. The apparent overlap of speech and voice responses in prior studies may be due to coarse neuroimaging methods and analyses.

Component modeling: Strengths, limitations, and relationship to prior methods

Component modeling provides a way to (1) infer prominent response patterns,^{21,66} (2) suggest novel hypotheses, and (3) disentangle spatially overlapping responses.⁶⁷ Our results illustrate each of these benefits. We inferred a small number of components that explained much of the response variation across hundreds of electrodes. We uncovered a novel form of music selectivity (song selectivity) that we did not a priori expect. And the song-selective component showed clearer selectivity for singing than that present in individual electrodes, many of which appeared to reflect a mixture of music, speech, and song selectivity.

The key challenge of component modeling is that matrix approximation is ill-posed, and hence, the solution depends on statistical assumptions. Many component methods rely on just one of the following three assumptions: (1) non-negativity,⁶⁸ (2) sparsity across time or space,^{69,70} or (3) temporal smoothness.^{71,72} We showed that all of these properties are evident in auditory ECoG responses, and the model we developed to embody these assumptions predicted ECoG responses better than baseline models. Our key finding of song selectivity was nonetheless robust to these assumptions: song selectivity was observed in a model that only imposed non-negativity on the responses (Figure S2A), as well as a simpler, regression-based analysis (Figure 3) and in responses of individual electrodes (Figure 6), neither of which depend on statistical assumptions like non-negativity or sparsity.

Our fMRI decomposition method placed statistical constraints on the voxel weights because we had thousands of voxels (>10,000) with which to estimate statistics. Here, we additionally constrained the component responses because we had many fewer electrodes and high-dimensional response time courses. Our method is distinct from a variety of other relevant component models. Unlike many sparse convolutional models,⁷³ each component in our model is defined by a single time course and a single pattern of electrode weights rather than by a time-varying spatial pattern. As a result, our components can be more easily interpreted as the response of an underlying neuronal population. Unlike clustering methods (or convex NMF²¹), our method can disentangle responses that overlap within individual electrodes. And unlike many tensor decomposition methods,⁷⁴ our method does not require the shape of a component's

response time course to be identical across different stimuli, which is critical when modeling responses to sensory features that are not necessarily aligned to stimulus onset.

Combining the strengths of fMRI and ECoG data

fMRI and ECoG data have different strengths and weaknesses. fMRI data are coarse due to the indirect sampling of neural activity via blood flow but are non-invasive and can provide dense, comprehensive coverage from many subjects. By contrast, ECoG coverage is sparse and driven by clinical demands, but has much better spatiotemporal precision. Our study introduces a method for combining the strengths of ECoG and fMRI, by inferring a set of canonical response patterns with ECoG and then mapping their spatial distribution with fMRI. This approach cannot spatially distinguish two components with similar time-averaged responses (e.g., the speech-selective components C1 and C15), but empirically, most components had distinct time-averaged responses, and we found a close correspondence between fMRI and ECoG maps, which was primarily limited by the sparse coverage of ECoG recordings (Figure 2C).

CONCLUSIONS

By revealing a neural population selective for song, our study begins to unravel the neural code for music, raising many questions for future research. Do music- and song-selective responses reflect note-level structure (e.g., pitch and timbre)⁷⁵ or the way notes are patterned (e.g., melodies and rhythms)?⁷⁶ How can music and song selectivity be described in computational terms, given that standard acoustic features appear insufficient?¹⁰ And how did music and song selectivity arise over the course of development or evolution?^{1,2} Our study represents an initial step toward answering these longstanding questions.

STAR★METHODS

Detailed methods are provided in the online version of this paper and include the following:

- **KEY RESOURCES TABLE**
- **RESOURCE AVAILABILITY**
 - Lead contact
 - Materials availability
 - Data and code availability
- **EXPERIMENTAL MODEL AND SUBJECT DETAILS**
 - Subjects
- **METHOD DETAILS**
 - Electrode grids
 - Natural sounds
 - Modulation-matched synthetic sounds
 - Sound category assignments
 - Music ratings
- **QUANTIFICATION AND STATISTICAL ANALYSIS**
 - Preprocessing
 - Session effects
 - Electrode selection
 - Electrode localization
 - Response statistics relevant to component modeling
 - Component model

- Constraining the smoothing kernel
- Cross-validation analyses
- Assessing component robustness
- fMRI weight maps
- Tonotopic definition of primary auditory cortex
- Component responses to modulation-matched sounds
- Acoustic correlations and predictions
- Calculating latencies
- Speech STRFs
- Predicting ECoG components from fMRI and vice versa
- Hypothesis-driven component analysis
- Single electrode analyses
- Statistics
- Noise correction

SUPPLEMENTAL INFORMATION

Supplemental information can be found online at <https://doi.org/10.1016/j.cub.2022.01.069>.

ACKNOWLEDGMENTS

This work was supported by the National Institutes of Health (DP1 HD091947 to N.K., P41-EB018783 to P.B. and G.S., P50-MH109429 to G.S., R01-EB026439 to P.B. and G.S., U24-NS109103 to P.B. and G.S., U01-NS108916 to P.B. and G.S., R25-HD088157 to G.S., and K99DC018051-01A1 to S.V.N.-H.), the US Army Research Office (W911NF-15-1-0440 to G.S.), the National Science Foundation (grant BCS-1634050 to J.H.M.), the NSF Science and Technology Center for Brains, Minds, and Machines (CCF-1231216), Fondazione Neurone (grant to P.B. and G.S.), the Howard Hughes Medical Institute (LSRF Postdoctoral Fellowship to S.V.N.-H.), and the Kristin R. Pressman and Jessica J. Pourian '13 Fund at MIT.

AUTHOR CONTRIBUTIONS

Conceptualization, S.V.N.-H., J.F., P.B., A.R., J.H.M., G.S., and N.K.; methodology, S.V.N.-H., J.F., P.B., and A.R.; software, S.V.N.-H. and J.F.; validation, S.V.N.-H.; formal analysis, S.V.N.-H.; investigation, S.V.N.-H., D.B., P.B., and A.R.; resources, P.B. and A.R.; data curation, S.V.N.-H., J.F., D.B., and P.B.; writing – original draft, S.V.N.-H.; writing – review & editing, S.V.N.-H., J.F., D.B., P.B., A.R., J.H.M., G.S., and N.K.; visualization, S.V.N.-H.; supervision, A.R., J.H.M., G.S., and N.K.; project administration, N.K.; funding acquisition, S.V.N.-H., P.B., A.R., J.H.M., G.S., and N.K.

DECLARATION OF INTERESTS

N.K. was recently on the *Current Biology* advisory board. The other authors declare no competing interests.

Received: February 23, 2021
Revised: October 26, 2021
Accepted: January 24, 2022
Published: February 22, 2022

REFERENCES

1. Wallin, N.L., Merker, B., and Brown, S. (2001). *The Origins of Music* (MIT Press).
2. Mehr, S.A., Singh, M., Knox, D., Ketter, D.M., Pickens-Jones, D., Atwood, S., Lucas, C., Jacoby, N., Egner, A.A., Hopkins, E.J., et al. (2019). Universality and diversity in human song. *Science* 366, eaax0868.

3. Patel, A.D. (2019). Evolutionary music cognition: cross-species studies. In *Foundations in Music Psychology: Theory and Research*, P.J. Rentfrow, and D.J. Levitin, eds. (MIT Press), pp. 459–501.
4. Peretz, I., Vuvar, D., Lagrois, M.É., and Armony, J.L. (2015). Neural overlap in processing music and speech. *Philos. Trans. R. Soc. Lond. B Biol. Sci.* **370**, 20140090.
5. Leaver, A.M., and Rauschecker, J.P. (2010). Cortical representation of natural complex sounds: effects of acoustic features and auditory object category. *J. Neurosci.* **30**, 7604–7612.
6. Norman-Haignere, S.V., Kanwisher, N.G., and McDermott, J.H. (2015). Distinct cortical pathways for music and speech revealed by hypothesis-free voxel decomposition. *Neuron* **88**, 1281–1296.
7. Peretz, I. (2016). Neurobiology of congenital amusia. *Trends Cogn. Sci.* **20**, 857–867.
8. Peterson, R.L., and Pennington, B.F. (2015). Developmental dyslexia. *Annu. Rev. Clin. Psychol.* **11**, 283–307.
9. Herholz, S.C., and Zatorre, R.J. (2012). Musical training as a framework for brain plasticity: behavior, function, and structure. *Neuron* **76**, 486–502.
10. Kell, A.J.E., Yamins, D.L.K., Shook, E.N., Norman-Haignere, S.V., and McDermott, J.H. (2018). A task-optimized neural network replicates human auditory behavior, predicts brain responses, and reveals a cortical processing hierarchy. *Neuron* **98**, 630–644.e16.
11. Angulo-Perkins, A., Aubé, W., Peretz, I., Barrios, F.A., Armony, J.L., and Concha, L. (2014). Music listening engages specific cortical regions within the temporal lobes: differences between musicians and non-musicians. *Cortex* **59**, 126–137.
12. Boebinger, D., Norman-Haignere, S.V., McDermott, J.H., and Kanwisher, N. (2021). Music-selective neural populations arise without musical training. *J. Neurophysiol.* **125**, 2237–2263.
13. Casey, M.A. (2017). Music of the 7Ts: predicting and decoding multivoxel fMRI responses with acoustic, schematic, and categorical music features. *Front. Psychol.* **8**, 1179.
14. Humphries, C., Liebenthal, E., and Binder, J.R. (2010). Tonotopic organization of human auditory cortex. *NeuroImage* **50**, 1202–1211.
15. Da Costa, S.D., Zwaag, W. van der, Marques, J.P., Frackowiak, R.S.J., Clarke, S., and Saenz, M. (2011). Human primary auditory cortex follows the shape of Heschl's gyrus. *J. Neurosci.* **31**, 14067–14075.
16. Moerel, M., De Martino, F., and Formisano, E. (2012). Processing of natural sounds in human auditory cortex: tonotopy, spectral tuning, and relation to voice sensitivity. *J. Neurosci.* **32**, 14205–14216.
17. Baumann, S., Petkov, C.I., and Griffiths, T.D. (2013). A unified framework for the organization of the primate auditory cortex. *Front. Syst. Neurosci.* **7**, 11.
18. Schönwiesner, M., and Zatorre, R.J. (2009). Spectro-temporal modulation transfer function of single voxels in the human auditory cortex measured with high-resolution fMRI. *Proc. Natl. Acad. Sci. USA* **106**, 14611–14616.
19. Barton, B., Venezia, J.H., Saberi, K., Hickok, G., and Brewer, A.A. (2012). Orthogonal acoustic dimensions define auditory field maps in human cortex. *Proc. Natl. Acad. Sci. USA* **109**, 20738–20743.
20. Santoro, R., Moerel, M., De Martino, F., Goebel, R., Ugurbil, K., Yacoub, E., and Formisano, E. (2014). Encoding of natural sounds at multiple spectral and temporal resolutions in the human auditory cortex. *PLoS Comp. Biol.* **10**, e1003412.
21. Hamilton, L.S., Edwards, E., and Chang, E.F. (2018). A spatial map of onset and sustained responses to speech in the human superior temporal gyrus. *Curr. Biol.* **28**, 1860–1871.e4.
22. Belin, P., Zatorre, R.J., Lafaille, P., Ahad, P., and Pike, B. (2000). Voice-selective areas in human auditory cortex. *Nature* **403**, 309–312.
23. Overath, T., McDermott, J.H., Zarate, J.M., and Poeppel, D. (2015). The cortical analysis of speech-specific temporal structure revealed by responses to sound quilts. *Nat. Neurosci.* **18**, 903–911.
24. Mesgarani, N., Cheung, C., Johnson, K., and Chang, E.F. (2014). Phonetic feature encoding in human superior temporal gyrus. *Science* **343**, 1006–1010.
25. Di Liberto, G.M., O'Sullivan, J.A., and Lalor, E.C. (2015). Low-frequency cortical entrainment to speech reflects phoneme-level processing. *Curr. Biol.* **25**, 2457–2465.
26. de Heer, W.A., Huth, A.G., Griffiths, T.L., Gallant, J.L., and Theunissen, F.E. (2017). The hierarchical cortical organization of human speech processing. *J. Neurosci.* **37**, 6539–6557.
27. Brodbeck, C., Hong, L.E., and Simon, J.Z. (2018). Rapid transformation from auditory to linguistic representations of continuous speech. *Curr. Biol.* **28**, 3976–3983.e5.
28. Norman-Haignere, S.V., Long, L.K., Devinsky, O., Doyle, W., Irobunda, I., Merricks, E.M., Feldstein, N.A., McKhann, G.M., Schevon, C.A., Flinker, A., et al. (2022). Multiscale temporal integration organizes hierarchical computation in human auditory cortex. Preprint at *Nat. Hum. Behav.* Published online February 10, 2022. <https://doi.org/10.1038/s41562-021-01261-y>.
29. Norman-Haignere, S.V., and McDermott, J.H. (2018). Neural responses to natural and model-matched stimuli reveal distinct computations in primary and nonprimary auditory cortex. *PLoS Biol* **16**, e2005127.
30. Patterson, R.D., Uppenkamp, S., Johnsrude, I.S., and Griffiths, T.D. (2002). The processing of temporal pitch and melody information in auditory cortex. *Neuron* **36**, 767–776.
31. Penagos, H., Melcher, J.R., and Oxenham, A.J. (2004). A neural representation of pitch salience in nonprimary human auditory cortex revealed with functional magnetic resonance imaging. *J. Neurosci.* **24**, 6810–6815.
32. Norman-Haignere, S., Kanwisher, N., and McDermott, J.H. (2013). Cortical pitch regions in humans respond primarily to resolved harmonics and are located in specific tonotopic regions of anterior auditory cortex. *J. Neurosci.* **33**, 19451–19469.
33. Roswadowski, C., Kappes, C., Obrig, H., and von Kriegstein, K. (2018). Obligatory and facultative brain regions for voice-identity recognition. *Brain* **141**, 234–247.
34. Groen, I.I., Greene, M.R., Baldassano, C., Fei-Fei, L., Beck, D.M., and Baker, C.I. (2018). Distinct contributions of functional and deep neural network features to representational similarity of scenes in human brain and behavior. *eLife* **7**, e32962.
35. Merrill, J., Sammler, D., Bangert, M., Goldhahn, D., Lohmann, G., Turner, R., and Friederici, A.D. (2012). Perception of words and pitch patterns in song and speech. *Front. Psychol.* **3**, 76.
36. Tierney, A., Dick, F., Deutsch, D., and Sereno, M. (2013). Speech versus song: multiple pitch-sensitive areas revealed by a naturally occurring musical illusion. *Cereb. Cortex* **23**, 249–254.
37. Whitehead, J.C., and Armony, J.L. (2018). Singing in the brain: neural representation of music and voice as revealed by fMRI. *Hum. Brain Mapp* **39**, 4913–4924.
38. Sammler, D., Baird, A., Valabrègue, R., Clément, S., Dupont, S., Belin, P., and Samson, S. (2010). The relationship of lyrics and tunes in the processing of unfamiliar songs: a functional magnetic resonance adaptation study. *J. Neurosci.* **30**, 3572–3578.
39. Patel, A.D. (2011). In *Language, music, and the brain: a resource-sharing framework*, P. Rebuschat, M. Rohmeier, J.A. Hawkins, and I. Cross, eds., pp. 204–223. Oxford.
40. Sundberg, J. (1999). The perception of singing. In *The Psychology of Music* (Elsevier), pp. 171–214.
41. Arcaro, M.J., and Livingstone, M.S. (2021). On the relationship between maps and domains in inferotemporal cortex. *Nat. Rev. Neurosci.* **22**, 573–583.
42. Levy, I., Hasson, U., Avidan, G., Hendler, T., and Malach, R. (2001). Center-periphery organization of human object areas. *Nat. Neurosci.* **4**, 533–539.
43. Conway, B.R. (2018). The organization and operation of inferior temporal cortex. *Annu. Rev. Vis. Sci.* **4**, 381–402.
44. Lee, H., Margalit, E., Jozwik, K.M., Cohen, M.A., Kanwisher, N., Yamins, D.L., and DiCarlo, J.J. (2020). Topographic deep artificial neural networks reproduce the hallmarks of the primate inferior temporal cortex face

- processing network. Preprint at bioRxiv. <https://doi.org/10.1101/2020.07.09.185116>.
45. Blaich, N.M., Behrmann, M., and Plaut, D.C. (2022). A connectivity-constrained computational account of topographic organization in primate high-level visual cortex. *Proc. Natl. Acad. Sci. USA* *119*, e2112566119.
 46. Callan, D.E., Tsytarev, V., Hanakawa, T., Callan, A.M., Katsuhara, M., Fukuyama, H., and Turner, R. (2006). Song and speech: brain regions involved with perception and covert production. *Neuroimage* *31*, 1327–1342.
 47. Lévêque, Y., and Schön, D. (2015). Modulation of the motor cortex during singing-voice perception. *Neuropsychologia* *70*, 58–63.
 48. Zatorre, R.J., Chen, J.L., and Penhune, V.B. (2007). When the brain plays music: auditory-motor interactions in music perception and production. *Nat. Rev. Neurosci.* *8*, 547–558.
 49. Kleber, B.A., and Zarate, J.M. (2014). *The Neuroscience of Singing* (Oxford University Press).
 50. Hickok, G., Houde, J., and Rong, F. (2011). Sensorimotor integration in speech processing: computational basis and neural organization. *Neuron* *69*, 407–422.
 51. Guenther, F.H., and Vladusich, T. (2012). A neural theory of speech acquisition and production. *J. Neurolinguistics* *25*, 408–422.
 52. Bainbridge, C.M., Bertolo, M., Youngers, J., Atwood, S., Yurdum, L., Simson, J., Lopez, K., Xing, F., Martin, A., and Mehr, S.A. (2021). Infants relax in response to unfamiliar foreign lullabies. *Nat. Hum. Behav.* *5*, 256–264.
 53. Weiss, M.W., Trehub, S.E., and Schellenberg, E.G. (2012). Something in the way she sings: enhanced memory for vocal melodies. *Psychol. Sci.* *23*, 1074–1078.
 54. Blood, A.J., and Zatorre, R.J. (2001). Intensely pleasurable responses to music correlate with activity in brain regions implicated in reward and emotion. *Proc. Natl. Acad. Sci. USA* *98*, 11818–11823.
 55. Salimpoor, V.N., van den Bosch, I., Kovacevic, N., McIntosh, A.R., Dagher, A., and Zatorre, R.J. (2013). Interactions between the nucleus accumbens and auditory cortices predict music reward value. *Science* *340*, 216–219.
 56. Parvizi, J., Jacques, C., Foster, B.L., Witthoft, N., Rangarajan, V., Weiner, K.S., and Grill-Spector, K. (2012). Electrical stimulation of human fusiform face-selective regions distorts face perception. *J. Neurosci.* *32*, 14915–14920.
 57. Schalk, G., Kapeller, C., Guger, C., Ogawa, H., Hiroshima, S., Lafer-Sousa, R., Saygin, Z.M., Kamada, K., and Kanwisher, N. (2017). Facephenes and rainbows: causal evidence for functional and anatomical specificity of face and color processing in the human brain. *Proc. Natl. Acad. Sci. USA* *114*, 12285–12290.
 58. Dehaene, S., and Cohen, L. (2011). The unique role of the visual word form area in reading. *Trends Cogn. Sci.* *15*, 254–262.
 59. Froemke, R.C., Merzenich, M.M., and Schreiner, C.E. (2007). A synaptic memory trace for cortical receptive field plasticity. *Nature* *450*, 425–429.
 60. Mehr, S.A., and Krasnow, M.M. (2017). Parent-offspring conflict and the evolution of infant-directed song. *Evol. Hum. Behav.* *38*, 674–684.
 61. Tillmann, B. (2005). Implicit investigations of tonal knowledge in nonmusical listeners. *Ann. N. Y. Acad. Sci.* *1060*, 100–110.
 62. Bigand, E., and Poulin-Charronnat, B. (2006). Are we “experienced listeners”? A review of the musical capacities that do not depend on formal musical training. *Cognition* *100*, 100–130.
 63. Weiss, M.W., Schellenberg, E.G., Peng, C., and Trehub, S.E. (2019). Contextual distinctiveness affects the memory advantage for vocal melodies. *Auditory Percept. Cogn.* *2*, 47–66.
 64. Cohen, M.A., Alvarez, G.A., Nakayama, K., and Konkle, T. (2017). Visual search for object categories is predicted by the representational architecture of high-level visual cortex. *J. Neurophysiol.* *117*, 388–402.
 65. Belin, P., Zatorre, R.J., and Ahad, P. (2002). Human temporal-lobe response to vocal sounds. *Brain Res. Cogn. Brain Res.* *13*, 17–26.
 66. Chen, P.-H.C., Chen, J., Yeshurun, Y., Hasson, U., Haxby, J., and Ramadge, P.J. (2015). A reduced-dimension fMRI shared response model. *Advances in Neural Information Processing Systems* *28*, 460–468.
 67. de Cheveigné, A., and Parra, L.C. (2014). Joint decorrelation, a versatile tool for multichannel data analysis. *Neuroimage* *98*, 487–505.
 68. Lee, D.D., and Seung, H.S. (1999). Learning the parts of objects by non-negative matrix factorization. *Nature* *401*, 788–791.
 69. Olshausen, B.A., and Field, D.J. (1997). Sparse coding with an overcomplete basis set: a strategy employed by V1? *Vis. Res.* *37*, 3311–3325.
 70. Hyvärinen, A. (1999). Fast and robust fixed-point algorithms for independent component analysis. *IEEE Trans. Neural Netw.* *10*, 626–634.
 71. Wiskott, L., and Sejnowski, T.J. (2002). Slow feature analysis: unsupervised learning of invariances. *Neural Comput.* *14*, 715–770.
 72. Byron, M.Y., Cunningham, J.P., Santhanam, G., Ryu, S.I., Shenoy, K.V., and Sahani, M. (2009). Gaussian-process factor analysis for low-dimensional single-trial analysis of neural population activity. *Advances in Neural Information Processing Systems* *21*, 1881–1888.
 73. Bouchard, K.E., Bujan, A.F., Chang, E.F., and Sommer, F.T. (2017). Sparse coding of ECoG signals identifies interpretable components for speech control in human sensorimotor cortex. *Annu. Int. Conf. IEEE Eng. Med. Biol. Soc. 39th Annual International Conference of the IEEE Engineering in Medicine and Biology Society (EMBC) 2017*, 3636–3639.
 74. Williams, A.H., Kim, T.H., Wang, F., Vyas, S., Ryu, S.I., Shenoy, K.V., Schnitzer, M., Kolda, T.G., and Ganguli, S. (2018). Unsupervised discovery of demixed, low-dimensional neural dynamics across multiple timescales through tensor component analysis. *Neuron* *98*, 1099–1115.e8.
 75. Casey, M., Thompson, J., Kang, O., Raizada, R., and Wheatley, T. (2012). Population codes representing musical timbre for high-level fMRI categorization of music genres. In *Machine Learning and Interpretation in Neuroimaging* (Springer), pp. 34–41.
 76. Schindler, A., Herdener, M., and Bartels, A. (2013). Coding of melodic gestalt in human auditory cortex. *Cereb. Cortex* *23*, 2987–2993.
 77. Schalk, G., and Mellinger, J. (2010). *A Practical Guide to Brain-Computer Interfacing with BCI2000: General-Purpose Software for Brain-Computer Interface Research, Data Acquisition, Stimulus Presentation, and Brain Monitoring* (Springer Science & Business Media).
 78. Schalk, G., McFarland, D.J., Hinterberger, T., Birbaumer, N., and Wolpaw, J.R. (2004). BCI2000: a general-purpose brain-computer interface (BCI) system. *IEEE Trans. Biomed. Eng.* *51*, 1034–1043.
 79. Chi, T., Ru, P., and Shamma, S.A. (2005). Multiresolution spectrotemporal analysis of complex sounds. *J. Acoust. Soc. Am.* *118*, 887–906.
 80. Nichols, T.E., and Holmes, A.P. (2002). Nonparametric permutation tests for functional neuroimaging: a primer with examples. *Hum. Brain Mapp.* *15*, 1–25.
 81. Norman-Haignere, S.V., Albouy, P., Caclin, A., McDermott, J.H., Kanwisher, N.G., and Tillmann, B. (2016). Pitch-responsive cortical regions in congenital amusia. *J. Neurosci.* *36*, 2986–2994.
 82. Kuhn, H.W. (1955). The Hungarian method for the assignment problem. *Nav. Res. Logist. Q.* *2*, 83–97.
 83. Murphy, K.P. (2012). *Machine Learning: a Probabilistic Perspective* (MIT Press).
 84. Daube, C., Ince, R.A.A., and Gross, J. (2019). Simple acoustic features can explain phoneme-based predictions of cortical responses to speech. *Curr. Biol.* *29*, 1924–1937.e9.
 85. Efron, B. (1982). *The Jackknife, the Bootstrap, and Other Resampling Plans* (Siam).
 86. Loftus, G.R., and Masson, M.E. (1994). Using confidence intervals in within-subject designs. *Psychon. Bull. Rev.* *1*, 476–490.
 87. Schoppe, O., Harper, N.S., Willmore, B.D., King, A.J., and Schnupp, J.W. (2016). Measuring the performance of neural models. *Front. Comp. Neurosci.* *10*, 10.
 88. Spearman, C. (1910). Correlation calculated from faulty data. *Br. J. Psychol.* *3*, 271–295.

STAR★METHODS

KEY RESOURCES TABLE

REAGENT or RESOURCE	SOURCE	IDENTIFIER
Deposited data		
fMRI dataset of 165 natural sounds (10 subjects), Norman-Haignere et al. ⁶	McDermott, Kanwisher, and Norman-Haignere labs	https://github.com/snormanhaignere/natsound165-neuron2015
Software and algorithms		
Freesurfer	MGH	https://surfer.nmr.mgh.harvard.edu
Other		
165 natural sounds, Norman-Haignere et al. ⁶	McDermott, Kanwisher, and Norman-Haignere labs	http://mcdermottlab.mit.edu/svnh/Natural-Sound/Stimuli.html

RESOURCE AVAILABILITY

Lead contact

Requests for additional information or resources related to the study should be directed to Sam Norman-Haignere (samuel_norman-haignere@urmc.rochester.edu).

Materials availability

This study did not generate new unique reagents.

Data and code availability

- Source data is available in this repository: <https://github.com/snormanhaignere/song-ecog-current-biology>
- Code implementing the component decomposition is in this repository: <https://github.com/snormanhaignere/ecog-component-model>

EXPERIMENTAL MODEL AND SUBJECT DETAILS

Subjects

Fifteen epilepsy patients participated in our study (mean age: 35 years, age standard deviation: 14 years; 8 right-handed; 8 female). All subjects were native English speakers, born in the US, who did not speak a second language. These subjects underwent temporary implantation of subdural electrode arrays at Albany Medical College to localize the epileptogenic zones and to delineate these zones from eloquent cortical areas before brain resection. All subjects gave informed written consent to participate in the study, which was approved by the Institutional Review Board of Albany Medical College.

METHOD DETAILS

Electrode grids

Most subjects had electrodes implanted in a single hemisphere, and STG coverage was much better in one of the two hemispheres in all subjects (8 right hemisphere patients and 7 left hemisphere patients). In most subjects, electrodes had a 2.3 mm exposed diameter with a 6 mm center-to-center spacing for temporal lobe grids (10 mm spacing for grids in frontal, parietal and occipital lobe, but electrodes from these grids typically did not show reliable sound-driven responses; electrodes were embedded in silicone; PMT Corp., Chanhassen, MN). Two subjects were implanted with a higher-density grid (1 mm exposed diameter, 3 mm center-to-center spacing). One subject was implanted with stereotactic electrodes instead of grids.

Natural sounds

The sound set was the same as in our prior study.⁶ To generate the stimulus set, we began with a set of 280 everyday sounds for which we could find a recognizable, 2-second recording. Using an online experiment (via Amazon's Mechanical Turk), we excluded sounds that were difficult to recognize (below 80% accuracy on a ten-way multiple-choice task; 55–60 subjects for each sound), yielding 238 sounds. We then selected a subset of 160 sounds that were rated as most frequently heard in everyday life (in a second Mechanical Turk study; 38–40 ratings per sound). Five additional “foreign speech” sounds were included (“German,” “French,”

“Italian,” “Russian,” “Hindi”) to distinguish responses to acoustic speech structure from responses to linguistic structure (the 160-sound set included only two foreign speech stimuli: “Spanish” and “Chinese”). In total, there were 10 English speech stimuli, 7 foreign speech stimuli, 21 instrumental music stimuli, and 11 music stimuli with singing (see [sound category assignments](#)). Sounds were RMS-normalized and presented by BCI2000^{77,78} at a comfortable volume using sound-isolating over-the-ear headphones (Panasonic RP-HTX7, 10 dB isolation). The sound set is freely available: <http://mcdermottlab.mit.edu/svnh/Natural-Sound/Stimuli.html>

Subjects completed between three and seven runs of the experiment (S11, S13: 3 runs, S6, S14: 4 runs, S15: 5 runs, S1: 7 runs; all other subjects: 6 runs). In each run, each natural sound was presented at least once. Between 14 and 17 of the sounds were repeated exactly back-to-back, and subjects were asked to press a button when they detected this repetition. This second instance of the sound was excluded from the analysis because the presence of a target could otherwise bias responses in favor of the repeated stimuli. Each run used a different random ordering of stimuli. There was a 1.4–2 second gap (randomly chosen) between consecutive stimuli.

Modulation-matched synthetic sounds

In ten subjects, we also measured responses to a distinct set of 36 natural sounds and 36 corresponding synthetic sounds that were individually matched to each natural sound in their spectrotemporal modulations statistics using the approach described in our prior study.²⁹ The synthesis algorithm starts with an unstructured noise stimulus and iteratively modifies the noise to match the modulation statistics of a natural sound. Modulations are measured using a standard model of auditory cortical responses⁷⁹ in which a cochleagram is passed through a set of linear filters tuned to modulations at a particular audio frequency, temporal rate, and spectral scale (i.e. how coarse vs fine the modulations are in frequency). The spectrotemporal filters were created by crossing 9 temporal rates (0.5, 1, 2, 4, 8, 16, 32, 128 Hz) with 7 spectral scales (0.125, 0.25, 0.5, 1, 2, 4, 8 cycles per octave) and replicating each filter at each audio frequency. The synthesis procedure alters the noise stimulus to match the histogram of response magnitudes across time for each filter in the model, which implicitly matches all time-averaged statistics of the filter responses (e.g., mean, variance, skew). The stimuli and synthesis procedures were very similar to those used in our prior study with a few minor exceptions that are noted next.

All stimuli were 4 seconds. We used shorter stimuli than the 10-second stimuli in our prior fMRI study due to limitations in the recording time. Because the stimuli were shorter, we did not include the very low-rate filters (0.125 and 0.25 Hz), which were necessary for longer stimuli to prevent energy from clumping unnaturally at particular moments in the synthetic recording. We also did not include “DC filters” but instead simply matched the mean value of the cochleagram across time and frequency at each iteration of the algorithm. Our prior paper described two versions of the algorithm: one in which the histogram-matching procedure was applied to the raw filter outputs and one where the matching procedure was applied to the envelopes of the filter responses. We found that the resulting stimuli were very similar, both perceptually and in terms of the cortical response. The stimuli tested here were created by applying the histogram matching procedure to the envelopes.

The stimuli were presented in random order with a 1.4- to 1.8-second gap between stimuli (for the first subject tested, a 2- to 2.2-second gap was used). The natural sounds were repeated to make it possible to assess the reliability of stimulus-driven responses. For all analyses, we simply averaged responses across the two repetitions. The sound set was presented across 4 runs. In one subject (S1), the entire experiment was repeated once.

Sound category assignments

In an online experiment, Mechanical Turk subjects chose the category that best described each of the 165 sounds tested, and we assigned each sound to its most frequently chosen category (30–33 subjects per sound).⁶ Category assignments were highly reliable (split-half kappa = 0.93). We chose to re-assign three sounds (“cymbal crash”, “horror film sound effects”, and “drum roll”) from the “instrumental music” category to a new “sound effects” category. There were two motivations for this re-assignment: (1) these three sounds were the only sounds assigned to the music category that produced weak fMRI responses in the music-selective component we inferred in our prior study,⁶ presumably because they lack canonical types of musical structure (i.e. clear notes, melody, rhythm, harmony, key, etc.); and (2) excluding these sounds made our song selectivity contrast (sung music – (instrumental music + speech)) more conservative as it is not biased upwards by the presence of instrumental music sounds that lack rich musical structure.

Music ratings

We used a large collection of online ratings (188 subjects) collected in a prior study¹² to compare the instrumental and sung music in our study in terms of familiarity, musicality, and likeability. We found that the distributions of these ratings were highly overlapping for instrumental and sung music, with no significant difference between the categories ($p > 0.05$ via bootstrapping across sounds). Since the song-selective component responded strongly to every sung music stimulus and weakly to every instrumental music stimulus, its response is unlikely to reflect these variables.

QUANTIFICATION AND STATISTICAL ANALYSIS

Preprocessing

Preprocessing was implemented in MATLAB. The scripts used to implement the preprocessing steps are available here (we reference specific scripts within these directories in describing our analyses): <https://github.com/snormanhaignere/ecog-analysis-code> and <https://github.com/snormanhaignere/general-analysis-code>

The responses from all electrodes were common-average referenced to the grand mean across all electrodes (separately for each subject). We excluded noisy electrodes from the common-average reference by detecting anomalies in the 60 Hz power (see `channel_selection_from_60Hz_noise.m`; an IIR resonance filter with a 3dB down bandwidth of 0.6 Hz was used to measure the RMS power). Specifically, we excluded electrodes whose 60 Hz power exceeded 5 standard deviations of the median across electrodes. Because the standard deviation is itself sensitive to outliers, we estimated the standard deviation using the central 20% of samples, which are unlikely to be influenced by outliers (by dividing the range of the central 20% of samples by that which would be expected from a Gaussian of unit variance; see `zscore_using_central_samples.m`). After common-average referencing, we used a notch filter to remove 60 Hz noise and its harmonics (60, 120, 180, and 240 Hz; see `notch_filt.m`; an IIR notch filter with a 3dB down bandwidth of 1 Hz was used to remove individual frequency components; the filter was applied forward and backward using `filtfilt.m`).

We computed broadband gamma power by measuring the envelope of the preprocessed signal filtered between 70 and 140 Hz (see `bandpass_envelopes.m`; bandpass filtering was implemented using a 6th order Butterworth filter with 3dB down cutoffs of 70 and 140 Hz; the filter was applied forward and backward using `filtfilt.m`). The envelope was measured as the absolute value of the analytic signal after bandpassing. For single-electrode analyses (Figure 6), we downsampled the envelopes to 100 Hz (from the 1200 Hz recording rate) and smoothed the time courses with a 50 ms FWHM kernel to reduce noise and make it easier to distinguish the time courses for different categories in the plots. For component analyses, we downsampled the envelopes to 25 Hz, because this enabled us to fit the data in the limited memory available on the GPU used to perform the optimization. No smoothing was applied since the model inferred an appropriate smoothing kernel for each component.

Occasionally, we observed visually obvious artifacts in the broadband gamma power for a small number of timepoints. To detect these artifacts, we computed the 90th percentile of each electrode's response magnitudes across all timepoints, which is by definition near the upper end of that electrode's response distribution, but which should also be unaffected by outliers assuming the number of outliers accounts for less than 10% of time points (which we generally found to be the case). We classified a timepoint as an outlier if it exceeded 5 times the 90th percentile value for each electrode. We found this value to be relatively conservative in that only a small number of timepoints were excluded (<1% of timepoints for all sound-responsive electrodes), and the vast majority of the excluded timepoints were artifactual based on visual inspection of the broadband gamma time courses. Because there were only a small number of outlier timepoints, we replaced the outliers with interpolated values from nearby non-outlier timepoints. We also manually excluded 2 electrodes and one to three runs from 9 other electrodes where there were a large number of visually obvious artifacts.

For each 2-second stimulus, we measured the response of each electrode during a three-second window locked to sound onset (for the 4-second natural and modulation-matched stimuli we used a 5-second window). We detected the onset of sound in each stimulus by computing the waveform power in 10 ms bins (with a 2 ms hop) and selecting the first bin in which the audio power exceeded 50 dB of the maximum power across all windows and stimuli. Following standard practice, the audio and ECoG data were synced by sending a copy of the audio signal to the same system used to record ECoG signals. This setup allowed us to measure the time delay between when the system initiated a trial and the onset of sound (which we measured using pure tones).

Responses were converted to units of percent signal change relative to silence by subtracting and then dividing the response of each electrode by the average response during the 300 ms before each stimulus.

Session effects

For six of the 15 subjects, runs were collected across two sessions with a gap in between (typically a day; the 7th run of S1 was collected in a third session). For the vast majority of electrodes, we found that their response properties were stable across sessions. Occasionally, we observed electrodes that substantially changed their selectivity, potentially due to small changes in the positioning of the electrodes over the cortex. To identify such changes, we measured the time-averaged response of each electrode to each of the 165 sounds tested for each run of data. We then detected electrodes for which the test-retest correlation from runs of the same session was significantly greater than the test-retest correlation from runs of different sessions ($p < 10^{-5}$; we used time-averaged response profiles rather than the raw time courses because we found them to be more reliable, and thus a better target for detecting selectivity changes across sessions; for S1 we grouped the runs from the 2nd and 3rd session together since there was only a single run in the 3rd session). Significance was evaluated via a permutation test⁸⁰ in which we permuted the correspondence between stimuli across runs (10,000 permutations). We used this approach to build up a null distribution for our test statistic (the difference between the correlation within and across sessions), fit this null distribution with a Gaussian (so that we could estimate small p-values that would have been impossible to estimate via counting), and used the null to calculate a two-sided p-value (by measuring the tail probability that exceeded the test statistic and multiplying by 2). Seven electrodes passed our conservative significance threshold. For these electrodes, we simply treated the data from different sessions as coming from different electrodes, since they likely sampled distinct neural populations.

Electrode selection

We selected electrodes with a reliable response across the 165 natural sounds tested. Specifically, we separately measured each electrode's broadband gamma response time course using odd vs. even runs/repetitions (each sound was presented once per run, ignoring 1-back repetitions which were discarded; see [natural sounds](#) above). We then correlated each electrode's full response time course across all sounds between these two repeated measurements. We kept all electrodes with a split-half correlation greater than 0.2 (electrodes with a test-retest correlation less than 0.2 were quite noisy upon inspection). Results were similar using a more liberal threshold of 0.1.

Electrode localization

We localized electrodes in order to visualize the electrode weights for each component. Electrode locations played no role in the identification of components or category-selective electrodes.

Following standard practice, we identified electrodes as bright spots on a post-operative computer tomography (CT) image. The CT was aligned to a high-resolution, pre-operative magnetic resonance image (MRI) using a rigid-body transformation. We then projected each electrode onto the cortical surface, computed by Freesurfer from the MRI scan. This projection is error-prone because far-away points on the cortical surface can be spatially nearby due to cortical folding. As a consequence, it was not uncommon for electrodes very near STG, where sound-driven responses are common, to be projected to a spatially nearby point on the middle temporal or supramarginal/inferior frontal gyrus, where sound-driven responses are much less common (Figures S7A and S7B). To minimize gross errors, we preferentially localized sound-driven electrodes to regions where sound-driven responses are likely to occur²⁸ (Figure S7C). Specifically, using a recently collected fMRI dataset,¹² where responses were measured to the same 165 sounds in a large cohort of 20 subjects with whole-brain coverage (our prior published study only had partial brain coverage⁶), we calculated the fraction of subjects that showed a significant response to sound at each point in the brain ($p < 10^{-5}$, measured using a permutation test⁸¹). We treated this map as a prior and multiplied it by a likelihood map, computed separately for each electrode based on the distance of that electrode to each point on the cortical surface (using a Gaussian error distribution; 10 mm FWHM). We then assigned each electrode to the point on the cortical surface where the product of the prior and likelihood was greatest (which can be thought of as the maximum posterior probability solution). We smoothed the prior probability map so that it would only affect the localization of electrodes at a coarse level (10 mm FWHM kernel), and not bias the location of electrodes locally, and we set the minimum prior probability to be 0.05 to ensure every point had non-zero prior probability.

Response statistics relevant to component modeling

Our component model approximated the response of each electrode as the weighted sum of a set of canonical response time courses (“components”). The component time courses are shared across all electrodes, but the weights are unique. We modeled each electrode as the weighted sum of multiple components because each electrode reflects the pooled activity of many neurons. Our analysis is a form of matrix factorization in which the data matrix, consisting of all the electrode responses, is approximated as a product of a component response matrix and a component weight matrix.

Matrix factorization is inherently ill-posed in that there exist many equally good approximations. Thus, we constrained our factorization by additional statistical criteria. Most component methods rely on one of three statistical assumptions: (1) non-negativity;⁶⁸ (2) a non-Gaussian (typically sparse) distribution of response magnitudes across time or space;^{69,70} or (3) temporal smoothness of the component responses.^{71,72} We investigated each of these statistical properties in broadband gamma responses to sound (Figures S1A–S1D) in order to determine which statistics might be useful in designing an appropriate factorization method.

To evaluate non-negativity, we measured the percent of the total RMS power accounted for by positive vs. negative responses during the presentation of sound (measured relative to 300 ms of silence preceding the onset of each sound):

$$100 * \sqrt{\frac{\sum_i p_i^2}{\sum_i p_i^2 + \sum_j n_j^2}} \quad (\text{Equation 3})$$

where $\{p_i\}$ and $\{n_j\}$ indicate the set of all positive and negative values for a given collection of response time courses. We applied the above equation to the pooled response time courses of all sound-responsive electrodes (pooling across all time-points, sounds, and electrodes) (Figure S1A). To minimize the effect of measurement noise, which could create negative values even if none are present (since measurement noise will not depend on the stimulus and thus noise fluctuations will be symmetric around the silent baseline), we measured the response of all electrodes in two splits of data (the average across odd and even runs). We then: (1) created an ordered list of response magnitudes, with the order determined by responses from the first split and the magnitudes given by the responses in the second split (2) applied a median filter to the ordered response magnitudes thus suppressing unreliable response variation (filter size = 10,000 datapoints) (see Figure S1A). Noise will cause the ordering of response magnitudes to change across splits and the median filter will suppress this variation. When Equation 3 was applied to these de-noised response distributions, we found that positive responses accounted for greater than 99.9% of the RMS power across all sound-responsive electrodes. Note that sound-responsive electrodes were selected based on the reliability of their responses, not based on a greater response to sounds compared with silence, and thus our analysis is not biased by our selection criterion.

To investigate whether and how the distribution of responses might differ from a Gaussian, we measured the skewness (normalized 3rd moment) and sparsity (excess kurtosis relative to a Gaussian, logarithmically transformed) of the responses:

$$\text{skewness} = \frac{\frac{1}{N} \sum_{i=1}^N (X_i - \bar{X})^3}{\left(\frac{1}{N} \sum_{i=1}^N (X_i - \bar{X})^2 \right)^{3/2}} \quad (\text{Equation 4})$$

$$\text{sparsity} = \log \left[\frac{\frac{1}{N} \sum_{i=1}^N (x_i - \bar{x})^4}{\left(\frac{1}{N} \sum_{i=1}^N (x_i - \bar{x})^2 \right)^2} - 3 \right] \quad (\text{Equation 5})$$

We applied the above equations to the response distribution of each electrode (pooling across all timepoints and sounds), denoised using the same procedure described in the preceding paragraph (median filter size = 100 bins). [Figure S1C](#) plots a histogram of these skewness and sparsity values across all electrodes. We found that all electrodes were skewed and sparse relative to a Gaussian, and relative to what would be expected given the statistics of ECoG noise ($p < 0.001$ via a sign test; see [statistics](#) for details). This observation implies that the response distribution of each electrode across time/stimuli has a heavy rightward tail, with a relatively small fraction of timepoints yielding large responses for any given electrode.

We also tested the skewness and sparsity of responses across electrodes. Specifically, we measured the average response of each electrode to each sound, and then for each sound, we applied [Equations 4 and 5](#) to the distribution of responses across the 271 sound-responsive electrodes. [Figure S1D](#) plots histograms of these skewness and sparsity measures across all 165 sounds. We did not apply our de-noising procedure since we only had 271 electrodes which made the sorting/median-filtering procedure infeasible (in contrast, for each electrode we had 12,375 timepoints across all sounds); moreover, time-averaging the response of each electrode to each sound helped to reduce noise. We again found that this distribution was significantly skewed and sparse relative to a Gaussian and relative to what would be expected given just noise in the data ($p < 0.001$ via sign test).

Finally, to investigate the temporal smoothness of auditory ECoG responses, we measured the normalized autocorrelation of each electrode's response ([Figure S1B](#)). To prevent noise from influencing the result, we correlated responses measured in independent runs (odd and even runs). This analysis revealed substantial long-term dependencies over more than a second, the strength of which varied substantially across electrodes.

Together, the results from our analysis revealed three key properties of auditory ECoG: (1) nearly all responses are positive/excitatory relative to sound onset; (2) responses are skewed/sparse across time/stimuli and electrodes; (3) responses are temporally smooth and the extent of this smoothness varies across electrodes. We sought to design a simple component model that captures these three essential properties.

Component model

In this section, we give a complete description of our component model, repeating some of the text and equations from the Results for completeness. Each electrode is represented by its response time course across all sounds ($\mathbf{e}_i(t)$) ([Figure S1E](#)). We approximate this response time course as the weighted sum of K component response time courses ($\mathbf{r}_k(t)$) (this is the same as [Equation 1](#) in the main text):

$$\mathbf{e}_i(t) \approx \sum_{k=1}^K w_{ik} \mathbf{r}_k(t)$$

The component time courses are shared across all electrodes, but the weights are specific to each electrode, allowing the model to approximate different response patterns. We constrain all of the component responses and weights to be positive. To encourage the components to be both sparse and smooth, we model the response time course of each component as the convolution of a set of sparse activations ($\mathbf{a}_k(t)$) with a smoothing kernel ($\mathbf{h}_k(t)$) (this is the same as [Equation 2](#) in the main text):

$$\mathbf{r}_k(t) = \mathbf{a}_k(t) * \mathbf{h}_k(t)$$

The inference algorithm proceeds by minimizing the cost function in [Equation 6](#), which has two parts: (1) a reconstruction penalty that encourages the model to be close to the data (the first term); and (2) an L1 penalty that encourages component sparsity (the second term).

$$\min_{\{w_{ik}\}, \{\mathbf{a}_k(t)\}, \{\mathbf{h}_k(t)\}} \frac{1}{I * T} \sum_{i=1}^I \sum_{t=1}^T \left(\mathbf{e}_i(t) - \sum_{k=1}^K w_{ik} \mathbf{r}_k(t) \right)^2 + \lambda \frac{1}{K * T} \sum_{k=1}^K \sum_{t=1}^T \mathbf{a}_k(t) \quad (\text{Equation 6})$$

The cost function in [Equation 6](#) was minimized subject to four sets of constraints: non-negativity of the electrode weights and activations, unimodality of the smoothing kernel, a fixed maximum value for each kernel, and a fixed L1 norm for the electrode weights. All the constraints were imposed by representing the constrained variable as a function of an unconstrained variable and performing optimization with respect to the unconstrained variables (in some cases, chaining together many such operations to impose more complex sets of constraints). Non-negativity was enforced by encoding the non-negative variable as the absolute value of an unconstrained real-valued variable. The operations used to enforce kernel unimodality are described in the next section and illustrated in [Figure S7E](#). The maximum value of each kernel was constrained by encoding the kernel as a latent variable divided by its maximum value. The L1 norm constraint was enforced by representing each electrode weight as a non-negative latent variable (itself represented as the absolute value of an unconstrained real-valued latent variable) divided by the mean of these latent variables across all electrodes and components. We note that the scale of activations and electrode weights are interchangeable, and we therefore

fixed the L1 norm of the electrode weights and penalized the activations. Both the constraint and penalty have the effect of encouraging sparsity.

We allowed the smoothing kernel to vary across components to capture the fact that different electrodes have variable levels of smoothness (Figure S1B). The learned smoothing kernels for each component are shown in Figure S7D. The kernels vary substantially in their extent/duration, thus capturing varying levels of smoothness across components. The model has two hyper-parameters: the number of components (K) and the strength of the sparsity penalty (λ), which we chose using cross-validation (see next section).

We implemented and optimized the model in TensorFlow (version 1.1.0), which provides efficient, general-purpose routines for optimizing models composed of common mathematical operations. We used the built-in ADAM optimizer to minimize the loss. We ran the optimizer for 10,000 iterations, decreasing the step size after every 2,000 iterations (in logarithmically spaced intervals; from 0.01 to 0.0001). Positivity of the activations and electrode weights was enforced by representing each element as the absolute value of a real-valued latent variable.

The components were numbered based on their total contribution to explaining the data matrix, measured by summing the response time course and electrode weights for each component, and then multiplying them together:

$$\left(\sum_i w_{ik}\right) \left(\sum_t r_k(t)\right) \quad (\text{Equation 7})$$

Constraining the smoothing kernel

We investigated three methods for constraining the kernel to be smooth: (1) using a parametric kernel (e.g., Gamma distribution); (2) placing a penalty on the derivative of the kernel; and (3) constraining the kernel to be unimodal. We found that the optimizer had difficulty minimizing the loss when using parametric kernels. We found that penalizing the derivative and constraining the kernel to be unimodal were both effective (yielding similar cross-validated prediction accuracy), but penalizing the derivative requires a third hyper-parameter that must be chosen with cross-validation, so we chose the unimodal constraint.

We constrained the kernel to be unimodal by placing two constraints on its derivative (approximated as the difference between adjacent samples): (1) the first N points of the derivative must be positive and the remaining points must be negative (which forces the kernel to go up and then down, but not oscillate; where N is any integer less than the total number of timepoints in the kernel) (2) the sum of the derivative must equal 0 (ensuring that the kernel starts and ends at zero). The set of operations used to implement these constraints in TensorFlow is illustrated in Figure S7E. Many of the learned smoothing kernels were asymmetric, with a rapid rise and a slower falloff (Figure S7D). There is nothing in the constraints that encourages asymmetry and so this property must reflect an asymmetry in the neural responses.

Cross-validation analyses

We used cross-validated prediction accuracy to determine the number of components and the sparsity parameter (Figures 1E and S1F), as well as to compare our model with several baseline models (Figure S1G). For the purposes of cross-validation, we divided the time courses for different sounds into cells, thus creating an electrode \times sound matrix of cells, each with a single time course (Figure 1E). We then trained the model on a random subset of 80% of cells and measured the model's prediction accuracy in the left-out 20% of cells (squared Pearson correlation between measured and predicted responses). We trained models starting from 10 different random initializations and selected the model (out of these 10) with the lowest error in the training data. We repeated our analyses using 5 different random splits of train and test data, averaging the test correlations across splits. For each split, we ensured an even and broad sampling of train and test stimuli using the following procedure: (1) we created a random ordering of stimuli and electrodes (2) we assigned the first 20% of sounds to be test sounds for the first electrode, the next 20% of sounds to be test sounds for electrodes 2, and so on. After using up all 165 sounds, we refreshed the pool of available test sounds using a new random ordering of stimuli.

To prevent correlated noise across electrodes from influencing the results, we used non-overlapping sets of runs (odd and even runs) for the training and test data (i.e., training on odd runs and testing on even runs, and vice-versa; again, averaging test correlations across the two splits in addition to averaging across the 5 splits of train/test cells described above). For a given set of hyper-parameters, we then averaged the test correlations across all electrodes to arrive at a summary measure of that model's performance (Figures 1E and S1F). We noise-corrected these correlations using the test-retest correlation of each electrode's response (see [noise correction](#) below).

We considered several baseline models that did not use the convolutional decomposition described above. We tested four baseline models: (1) we removed the sparseness and smoothness constraints entirely but maintained the non-negativity constraint (i.e. non-negative matrix factorization / NMF⁶⁸); (2) we imposed sparsity but not smoothness via an L1 penalty on the component responses (again fixing the L1 norm of the electrode weights) (3) we imposed smoothness but not sparsity via an L2 penalty on the derivative of the component responses (the first-order difference of adjacent time-points); and (4) we applied both the L1 sparsity and L2 smoothness constraint. To prevent the number of hyper-parameters from biasing the results, for each electrode, we selected the hyper-parameters that led to the best performance across electrodes from other subjects. We used grid-search over the following range of hyper-parameters: K (number of components) = [5, 10, 15, 20, 25, 30], λ (sparsity) = [0, 0.033, 0.1, 0.33, 1, 3.3], ω (smoothness) = [0, 0.033, 0.1, 0.33] (we verified that the best-performing models were not on the boundary of these values, except in cases

where the best-performing model had a parameter value of 0). We found that all of the baseline models performed significantly worse than our primary model (Figure S1G) ($p < 0.001$ via bootstrapping across subjects, see [statistics](#); including the model with both an L1 sparsity and L2 smoothness penalty, which had more hyper-parameters). This result suggests that our convolutional decomposition is an effective way of capturing both the smoothness and sparsity of auditory broadband gamma responses and is more effective than simply imposing sparsity and smoothing penalties directly on the component responses (and has fewer parameters).

Assessing component robustness

We first assessed if the components inferred by our main model were also present in a simpler model that only imposed non-negativity on the responses (using a 15-component model in both cases). We greedily matched components across models by correlating their electrode weights (results were the same if matching was performed using response profiles). The matching process started by matching the pair of components with the highest correlation, removing those two components, and then repeating this process until no more components were left. For the 10 most reliable components, the response profiles were qualitatively very similar (Figure S2A) and the correlation of response profiles and weights for corresponding components was high (all correlations > 0.84). Four components (C3, C5, C9, C13) were not included in the main figures because their responses or weights showed more substantial differences between models, leading to lower response or weight correlations (response correlations for these components: C5=0.69, C8=0.32, C9=0.13, C13=0.86; weight correlations: C5=0.79, C8=0.09, C9=-0.08, C13=0.82). These components are shown in Figure S2D.

To evaluate whether the components were robust across the number of model components, we tested if the same components were present in a 20-component model. We found that most of the components present in the 15-component model were also present in a 20-component model, demonstrating that the model primarily added new components without altering existing components. For the 10 most reliable components, the response profile and weight correlations between the components obtained for the 15- and 20-component models were always higher than 0.88. Reducing the number of components from 15 inevitably eliminated/merged some of the components from the 15-component model (which had the best cross-validated prediction accuracy), though we note that a song-selective component was still evident in a 10-component model.

For the 15-component model, we found that most components had weights that were broadly distributed across many electrodes and subjects. As we increased the number of components in the model, we found that the additional components began to weigh heavily on a small number of electrodes, often from a single subject, which may help explain why cross-validated prediction accuracy dropped for higher numbers of components (Figure 1E). One component (C12) from the 15-component model was not included in the main figures because much of its weight was concentrated in a single subject (Figures S2B and S2C). The response of this component is also plotted in Figure S2D.

As with any sparse component model, our cost function is not convex, and the optimization algorithm could potentially arrive at local optima, leading to unstable results across different random initializations of the algorithm. To address this issue, we ran the analysis many times (1,000 times), using different random initializations (activations and electrode weights were initialized with random samples from a truncated normal distribution; see Figure S7E for the structure and initialization of the smoothing kernels). One would hope to obtain components that are stable, i.e., that are consistently present for all solutions with low cost, which we quantified by correlating the component response profiles for the solution with the lowest cost with those for the 99 next-best solutions (using the “Hungarian algorithm” to determine the correspondence between components from different solutions⁸²). As a measure of stability, we computed the median correlation value for each component across the 99 next-best solutions. For all of the components, even those that were less reliable by other metrics, the median correlation was greater than 0.93, indicating that the algorithm was able to find a stable minimum.

fMRI weight maps

We took advantage of a relatively large dataset of fMRI responses to the same 165 sounds in order to get a second and more reliable estimate of the anatomical weight map for our ECoG components (Figures 2B and 5B), thus combining the broader and denser sampling available in fMRI with the more precise functional components derived from ECoG. The dataset consisted of responses from 30 subjects collected across two studies.^{6,12} The subjects had a wide range of musical expertise from almost none to many years of training. We have found that fMRI responses to natural sounds, including selective responses to music, are similar in subjects with and without musical training.¹² We thus pooled data across all 30 subjects unless otherwise noted. We limited our analyses to the same anatomical region of sound-responsive voxels that we used in our prior study.⁶

The fMRI weights were computed by approximating each voxel’s response as the weighted sum of the ECoG components after time-averaging their response. The weights were computed using ordinary linear regression, implemented by multiplying the fMRI response profile of each voxel by the pseudoinverse of the time-averaged ECoG component response matrix. The time-averaged responses of the speech-selective components (C1&C15) were highly correlated ($r=0.91$) which would have made the pseudoinverse unstable, and thus when calculating the weights for each speech-selective component we excluded the other speech-selective component from the calculation of the pseudoinverse. We averaged the weights across subjects to arrive at our group maps.

To evaluate the correspondence between the weight maps for the ECoG components derived from the ECoG versus fMRI data, we correlated weight maps for corresponding components and compared this correlation to that for mismatching components, as well as to the split-half reliability across subjects of the fMRI and ECoG maps alone (Figure 2C). Because ECoG coverage varies from patient to patient, we split the patients into two groups with a similar number of electrodes that were evenly distributed between

the left and right hemisphere when evaluating split-half reliability (for fMRI analyses we simply used a random split with an equal number of subjects from each of the two studies). Specifically, we considered all possible splits of the 15 ECoG patients into two groups. For each split, we computed the absolute difference between the total number of electrodes in each group as well as the absolute difference between the total number of electrodes between the left and right hemisphere of each group. We then selected the split where the sum of these two difference scores was minimal. For the optimal split, the first group had 78 right hemisphere electrodes and 58 left hemisphere electrodes across 5 patients. The second group had 68 right hemisphere electrodes and 68 left hemisphere electrodes across 10 patients.

In order to compare the fMRI and ECoG maps, we resampled both to a common anatomical grid on the cortical surface (1.5 mm x 1.5 mm spacing). Because ECoG coverage varies, some grid positions are much better sampled than others. To account for this, we weighted each grid position by a measure of the total number of electrodes near to it when computing correlations. We did this for all correlations including the fMRI split-half correlations, where this is not necessary, so that the results would be comparable. The weighted Pearson correlation was computed by simply replacing the standard covariance, variance, and mean statistics with their weighted counterparts:

$$\text{corr}_w = \frac{\text{cov}_w(x, y)}{\sqrt{\text{var}_w(x)\text{var}_w(y)}} \quad (\text{Equation 8})$$

$$\text{cov}_w(x, y) = \frac{\sum_i w_i (x_i - \text{mean}_w(x))(y_i - \text{mean}_w(y))}{\sum_i w_i} \quad (\text{Equation 9})$$

$$\text{var}_w(x) = \frac{\sum_i w_i (x_i - \text{mean}_w(x))^2}{\sum_i w_i} \quad (\text{Equation 10})$$

$$\text{mean}_w(x) = \frac{\sum_i w_i x_i}{\sum_i w_i} \quad (\text{Equation 11})$$

The grid weights (w_i) were computed using the following equation:

$$w_i = \sum_{j=1}^N G(d_{ij}) \quad (\text{Equation 12})$$

where d_{ij} is the distance between grid position i and electrode j and $G(\cdot)$ is a Gaussian kernel (5 mm FWHM). A high grid weight indicates there were many nearby electrodes, while a low weight indicates there were no nearby electrodes. We excluded grid positions with a very small weight from the analysis ($w_i < 0.1$).

We bootstrapped across the fMRI subjects to get error bars for all correlations involving fMRI data (Figure 2C). To compute split-half correlations, we separately bootstrapped the subjects within each split. It was not feasible to bootstrap the ECoG subjects, because the spatial coverage was so variable. For the correlation matrices in Figure 2C, the components were arranged such that components with more similar response profiles were next to each other. The arrangement was computed using a hierarchical clustering algorithm (MATLAB's linkage function using a correlation distance metric).

Tonotopic definition of primary auditory cortex

We used tonotopic maps from a prior study⁶ to define primary auditory cortex at the group level. Specifically, we outlined by hand the tonotopic regions spanned by the high-low-high gradient characteristic of primary auditory cortex.^{14–17} Tonotopy was measured using responses to pure tones from one of six frequency ranges (center frequencies: 200, 400, 800, 1600, 3200, and 6400 Hz). We measured the frequency range that produced the maximum response in voxels significantly modulated by frequency ($p < 0.05$ in a 1-way ANOVA across the 6 ranges). These best-frequency maps were averaged across subjects to form group maps.

Component responses to modulation-matched sounds

The components were inferred using responses to just the 165 natural sounds from the main experiment. But since a subset of ten subjects were tested in both experiments, we could estimate the response of these same components to the natural and synthetic sounds from our control experiment. Specifically, we fixed the component electrode weights to the values inferred from the responses in our main experiment and learned a new set of component response time courses that best approximated the measured responses in the modulation-matching experiment. Since the electrode weights are known, this analysis is no longer ill-posed, and we thus removed all of the additional sparsity and smoothness constraints and simply estimated a set of non-negative response profiles that minimized the squared error between the measured and predicted response time courses (we left the non-negativity constraint because we found that nearly all of the measured responses were non-negative).

Acoustic correlations and predictions

We evaluated acoustic selectivity for the ECoG components that showed weak category selectivity and relatively similar responses to natural and modulation-matched sounds (Figure 5). Most of the response variance of these components could be explained by the first PC of the sound x time component response matrix, which for many of the components reflected a strong response at sound onset or offset, the magnitude of which varied across the sound set. We correlated the stimulus weights of the first PC (i.e., a measure of the response magnitude) with measures of frequency and spectrotemporal modulation energy. The frequency measures were the same as those used in Norman-Haignere et al.⁶ and were computed by summing energy in a cochleagram representation of sound across both time and frequency (within 6 coarse bands with center frequencies shown in Figure 5D), yielding one number per sound and frequency band. The modulation measures were the same as those used in Norman-Haignere and McDermott²⁹ and were computed using a standard bank of spectrotemporal modulation filters applied to a cochleagram representation of sound.^{29,79} This analysis yielded a 5D tensor (time x audio frequency x temporal modulation x spectral modulation x orientation). We measured the standard deviation across time of each filter's response and then averaged across audio frequency and orientation, yielding one number per sound and spectrotemporal modulation rate. We partialled out the contribution of the frequency measures from the modulation measures to ensure they could not explain any modulation correlations (using ordinary least squares regression).

We also measured the overall prediction accuracy of the modulation-based acoustic features, category labels, and the combination of the two (Figure S5). We again summarized the response of each ECoG component using its first PC and attempted to predict its response variation across stimuli. For the category-selective components, the first PC captured its selectivity for categories, allowing us to test whether this selectivity could be accounted for by standard acoustic features. We used all of the modulation features without averaging across frequency or orientation in order to give them the best possible chance to predict the data. We used ridge regularization to prevent overfitting and nested cross-validation to select the ridge parameter (5 folds; each category had a roughly equal number of sounds in each fold). The category labels were binary features indicating for each sound the category that it belonged to. We discarded two categories with fewer than 5 exemplars ("nature sounds" and "sound effects"). Acoustic features were z-scored and we equalized the norm of the acoustic and category features before combining them in our joint prediction model. For computational efficiency, the acoustic modulation features were compressed using the singular value decomposition. Given the SVD decomposition of the feature matrix:

$$F = USV^T \quad (\text{Equation 13})$$

The compressed matrix is given by:

$$F_{\text{compressed}} = US \quad (\text{Equation 14})$$

Since the number of acoustic features was greater than the number of sounds, this operation reduces the dimensionality of the feature set without losing any expressive power. Multiplying by S is important because it preserves the variance of each dimension, which plays an important role in regularizing the regression model.⁸³

Calculating latencies

We also calculated component latencies using the first PC of the sound x time response matrix for each component. Latencies were calculated as the time needed for the time course of the first PC to reach half of its maximum value.

Speech STRFs

The speech-selective components appeared to respond at different moments within each speech stimulus. To test if this variation was related to the stimulus, we used a traditional spectrotemporal receptive field (STRF) analysis (Figure S3). We estimated a linear mapping between the cochleagram for each sound and the ECoG component time course, fit in the standard way by regressing the response against delayed copies of each frequency channel. For each frequency regressor, we also included its half-wave rectified temporal derivative (difference between adjacent samples), which we found improved predictions, consistent with prior work.⁸⁴ The linear mapping was estimated using ridge regression, with 5-fold nested cross-validation across stimuli. Figures S3A and S3B plot the STRFs estimated for the speech-selective components (C1, C15) in response to just the speech stimuli (both English and foreign speech). Figure S3C shows the prediction of a STRF model trained to predict each component's response to all 165 sounds.

Predicting ECoG components from fMRI and vice versa

We tested if we could predict the response of the ECoG song-selective component from our previously inferred fMRI components (Figures S4A and S4B), and whether we could predict the response of the speech and music-selective fMRI components from our ECoG components (using all of the components from a 15-component model) (Figure 7). For these analyses, we averaged electrode responses across time. Predictions were made using ridge regression with five-fold cross-validation across the sound set. The regularization parameter was chosen using cross-validation within each training fold. The folds were chosen to include a roughly equal number of sounds from each category.

We used two independent measures of each fMRI and ECoG component to noise-correct the predictions and get a measure of explainable variance (see [noise correction](#) below). The two independent measurements were computed by first getting three independent measurements of each voxel or electrode response (from different stimulus repetitions). We used one measurement to

estimate a set of reconstruction weights that best approximated the component response (again using ridge regression). We then applied these reconstruction weights to the other two measurements of each electrode/voxel.

We also attempted to predict the response of the song-selective ECoG component (C11) from voxel responses to test if there was any song selectivity present in the original fMRI data that was not captured by components (Figures S4C and S4D). Analysis details were the same as described above, but the input was the response of all voxels from our two studies.^{6,12}

Hypothesis-driven component analysis

We used a hypothesis-driven regression analysis to directly test if there were components selective for speech, music, and singing in the data set (Figure 3). Specifically, we used ridge regression to try and learn a weighted sum of the electrode responses that yielded a binary response of 1 for all sounds from the target category and 0 for all other sounds. We used cross-validation across the sound set to prevent statistical circularity (nested 5-fold cross-validation with the ridge regularization parameter selected within the train set). We used time-averaged electrode responses to learn the weights since we only needed one number per sound to learn the mapping. We then multiplied the full time courses of the electrodes by the learned weights in order to be able to compare the component inferred by this analysis with the component inferred by our decomposition method.

Single electrode analyses

To identify electrodes selective for music, speech, and song, we defined a number of contrasts based on the average response to different categories. For example, to assess super-additive song selectivity we subtracted the summed response to instrumental music and speech from the response to sung music, and to be conservative we used the maximum response across English and foreign speech as our measure of the response to speech, yielding the following contrast: sung music – (max[English speech, foreign speech] + instrumental music). All of the individual contrasts tested are described in the Results (a greater-than sign is used instead of subtraction since we selected voxels where the contrast was greater than 0). We divided each contrast by the maximum response across all categories to compute a measure of selectivity.

In all cases, we used independent data to identify electrodes and measure their response. Specifically, we used two runs (first and last) to select electrodes and the remaining runs to evaluate their response. We note that we did not pre-select electrodes based on reliability, as was done for our decomposition analyses, in order to ensure that the data used to identify electrodes and measure their response was fully independent.

Statistics

The significance of all category contrasts was evaluated using bootstrapping.⁸⁵ Specifically, we sampled sounds from each category with replacement (100,000 times), averaged responses across the sampled sounds for each category, and then recomputed the contrast of interest (all of the contrasts tested are specified in the Results). We then counted the fraction of samples that fell below zero and multiplied by 2 to compute a two-sided p-value. For p-values smaller than 0.001, counting becomes unreliable, and so we instead fit the distribution of bootstrapped samples with a Gaussian and measured the tail probability that fell below zero (and multiplied by 2 to compute a two-sided p-value). For the component analyses, we corrected for multiple comparisons by multiplying these p-values by the number of components (i.e., Bonferroni correction).

We compared the song-selective component (C11) with the average response of all song-selective electrodes by counting the fraction of bootstrapped samples where the component showed greater super-additive selectivity for singing than the average response of the song-selective electrodes. The same approach was used to compare the song selectivity of the fMRI voxel predictions (Figures S4C and S4D) to (1) the song-selective ECoG component (2) the fMRI component predictions (Figures S4A and S4B) and (3) the acoustic feature predictions (Figure S5B).

We used fMRI to test for laterality effects because we had a large number of subjects with complete, bilateral coverage, unlike ECoG where each patient had sparse coverage from a single hemisphere. For each ECoG component, we computed the average weight of the top 100 voxels from the left and right hemisphere with the greatest weights along that component, corresponding to about 10% of sound responsive voxels (1040 voxels in the right hemisphere, 991 sound-responsive voxels in the left hemisphere). We focused on the top 100 voxels because component weights were generally concentrated in a small fraction of voxels. Results were robust to the specific number of voxels selected. We then subtracted the average weight for the left and right hemisphere and bootstrapped this difference score by sampling subjects with replacement (100,000 samples). We computed a p-value by counting the fraction of samples falling below or above zero (whichever was smaller) and multiplying by 2. We Bonferroni-corrected this p-value by multiplying by the number of components. We also tested if the song-selective component was significantly lateralized in the ECoG electrodes since there appeared to be a trend towards right lateralization. The number of electrodes in each hemisphere varied widely across subjects, so for this analysis, we simply bootstrapped the average weight difference between the two hemispheres (as opposed to trying to select the top N voxels). Laterality comparisons with ECoG are inevitably underpowered due to limited and variable coverage.

We also used bootstrapping across subjects to place error bars on the component model prediction scores. Specifically, we (1) sampled subjects with replacement (10,000 times); (2) averaged the correlation values across the electrodes from the sampled subjects; and (3) noise-corrected the correlation using the test-retest reliability of the sampled electrodes. We tested whether our component model outperformed our baseline models by counting the fraction of bootstrapped samples where the average predictions were lower than each baseline model and multiplying by 2 to arrive at a two-sided p-value. When plotting the predictions for different models (Figure S1G), we used “within-subject” error bars,⁸⁶ computed by subtracting off the mean of each bootstrapped

sample across all models before measuring the central 68% of the sampling distribution. We multiplied the central 68% interval by the correction factor shown below to account for a downward bias in the standard error induced by mean-subtraction⁸⁶:

$$\sqrt{\frac{N}{N-1}} \quad (\text{Equation 15})$$

We used a sign test to evaluate whether the response to natural sounds was consistently greater than responses to corresponding modulation-matched sounds. A sign test is a natural choice, because the natural and modulation-matched sounds are organized as pairs (Figure 4A). For components selective for speech or music (song-selective component described in the next paragraph), we compared the time-averaged response to natural speech/music with the corresponding modulation-matched controls (there were eight speech stimuli and eight instrumental music stimuli, and two music stimuli with singing). We performed the same analysis on the average response of speech- and music-selective electrodes (Figure 6C). For both components and electrodes, the response to natural sounds of the preferred category was always greater than the response to modulation-matched sounds, and thus significant with a sign test ($p < 0.01$).

Although there were only two music stimuli with singing in the modulation-matching experiment, the stimuli were relatively long (4 seconds). We thus subdivided the response to each stimulus into seven 500 ms segments (discarding the first 500 ms to account for the build-up in the response) and measured the average response to each segment. For both the song-selective component and the average response of song-selective electrodes, we found that for all fourteen 500-ms segments (7 segments across 2 stimuli), the response to natural sung music was higher than the response to the modulation-matched controls, and thus is significant with a sign test ($p < 0.01$).

To determine whether the electrode responses were significantly more skewed and sparse than would be expected given noise (i.e. to evaluate the significance of the skewness/sparsity measures described in [response statistics relevant to component modeling](#)), we computed the skewness/sparsity of two data quantities: (1) the residual error after subtracting the response to even and odd runs; and (2) the summed response across even and odd runs. The properties of the noise should be the same for these two quantities, but the second quantity will also contain the reliable stimulus-driven component of the response. Thus, if the second quantity (summed response) is more skewed/sparse than the first quantity (residual error), then the stimulus-driven response must be more skewed/sparse than the noise. To assess skewness/sparsity across time and stimuli, we measured the skewness and sparsity (Equations 4 and 5) separately for each electrode using the residual error and summed response (pooling responses across all time-points and stimuli). In every subject, we found that the average skewness/sparsity of the summed responses was greater than the skewness/sparsity of the residual error, and thus significant with a sign test ($p < 0.001$). We used the same approach to evaluate the skewness/sparsity of responses across electrodes, measured separately for each sound. Using a sign test across sounds, we found both the skewness and sparsity of the summed response to be significantly greater than that for the residual error ($p < 0.001$).

We used bootstrapping across sounds to place error bars on the measured prediction accuracies for the modulation-based acoustic features and category labels (as well as their combination) (Figure S5A). Specifically, we sampled sounds with replacement 100,000 times and re-measured the correlation between the measured and predicted response (significance and error bars were computed as already described).

We used a permutation test to evaluate if the speech STRFs (Figure S3) captured unique variance in the response of the two speech-selective components (C1 & C15). First, we calculated the Pearson correlation between the measured and STRF-predicted component response across all speech sounds (C1: $r = 0.79$, C15: $r = 0.82$). We then compared this correlation value with a null distribution, computed by permuting the correspondence across stimuli between the measured and predicted response (100,000 permutations). We also measured the correlation drop when we swapped the predictions across components (correlating the STRF for C1 with C15 and vice versa) and bootstrapped this drop score to test if it was significantly different from 0 (sampling sounds with replacement 100,000 times). P-values were computed by counting the fraction of permuted null samples that exceeded the target statistic or the fraction of bootstrapped drop scores that fell below 0. All tested comparisons were significant ($p < 0.01$).

Noise correction

We used standard noise correction procedures to provide a ceiling on our measured correlations and provide an estimate of explainable variance. In general, the correlation between two variables can be noise-corrected by dividing by the geometric mean of the reliability of the variables^{10,87}:

$$\frac{\text{corr}(x, y)}{\sqrt{\text{corr}(x_1, x_2)\text{corr}(y_1, y_2)}} \quad (\text{Equation 16})$$

where x_1 and x_2 are two independent measures of the same variable (same for y_1 and y_2). The numerator was computed by averaging the cross-variable correlations for two independent measurements:

$$\text{corr}(x, y) = 0.5 \text{corr}(x_1, y_1) + 0.5 \text{corr}(x_2, y_2) \quad (\text{Equation 17})$$

The correlations in Figure 2C are not noise-corrected and instead we explicitly plot the reliability ceiling (i.e., the denominator of Equation 16). When comparing ECoG and fMRI weight maps, we used all of the available data for computing the ECoG-fMRI

correlations (Figure 2C), and we, therefore, Spearman-Brown corrected the test-retest correlations that went into the reliability ceiling calculation since only half the data could be used to measure reliability⁸⁸:

$$\frac{2r}{1+r} \quad (\text{Equation 18})$$

where r is the uncorrected split-half correlation.

For simplicity, when measuring the response variance explained by the components (Figures 1E, S1F, and S1G), we only corrected for the reliability of the individual electrodes and not the component predictions, since the component predictions were much more reliable than the individual electrodes (i.e. we set the reliability of the component predictions to 1 in Equation 16).

We used the squared and noise-corrected Pearson correlation as a measure of explainable variance.

Current Biology, Volume 32

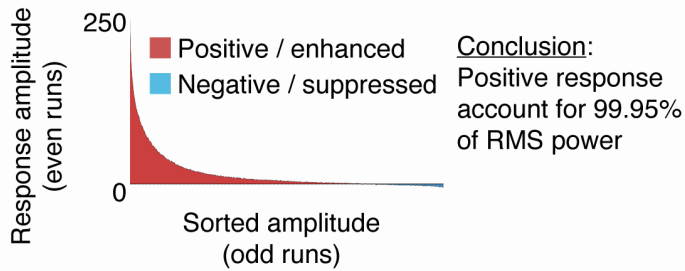
Supplemental Information

**A neural population selective for song
in human auditory cortex**

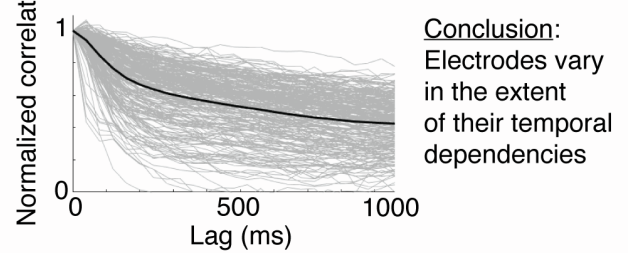
Sam V. Norman-Haignere, Jenelle Feather, Dana Boebinger, Peter Brunner, Anthony Ritaccio, Josh H. McDermott, Gerwin Schalk, and Nancy Kanwisher

Statistics relevant to component modeling

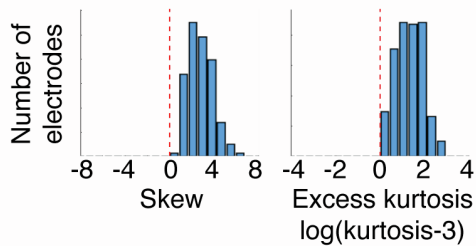
A Response amplitudes



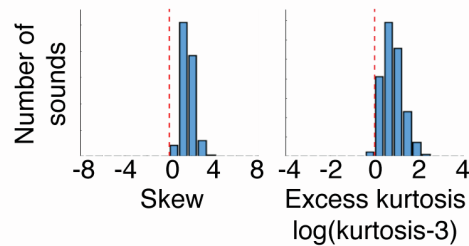
B Temporal autocorrelation



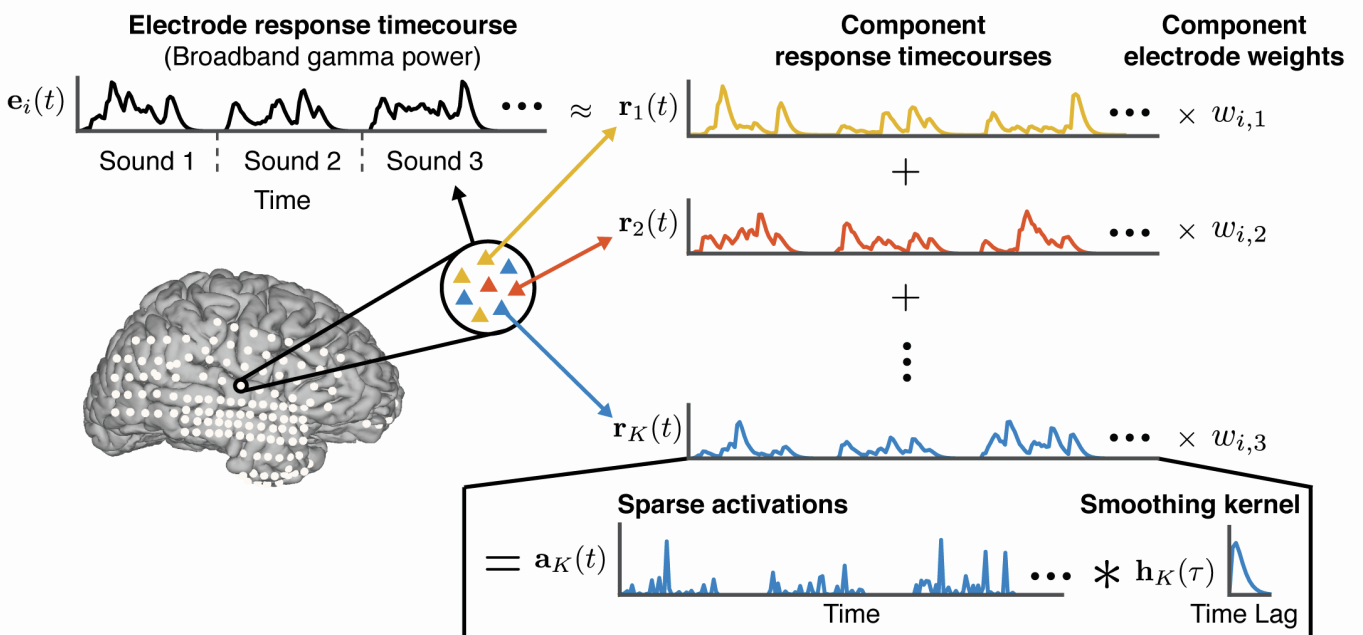
C Moments across time/stimuli



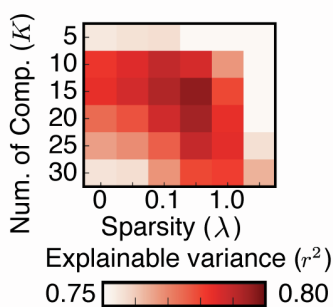
D Moments across electrodes



E Schematic of component model



F Hyper-parameters



G Model comparison

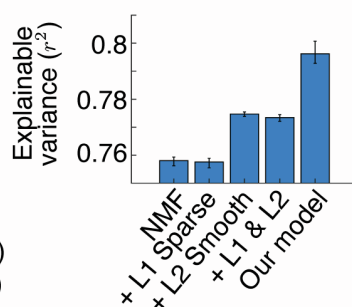
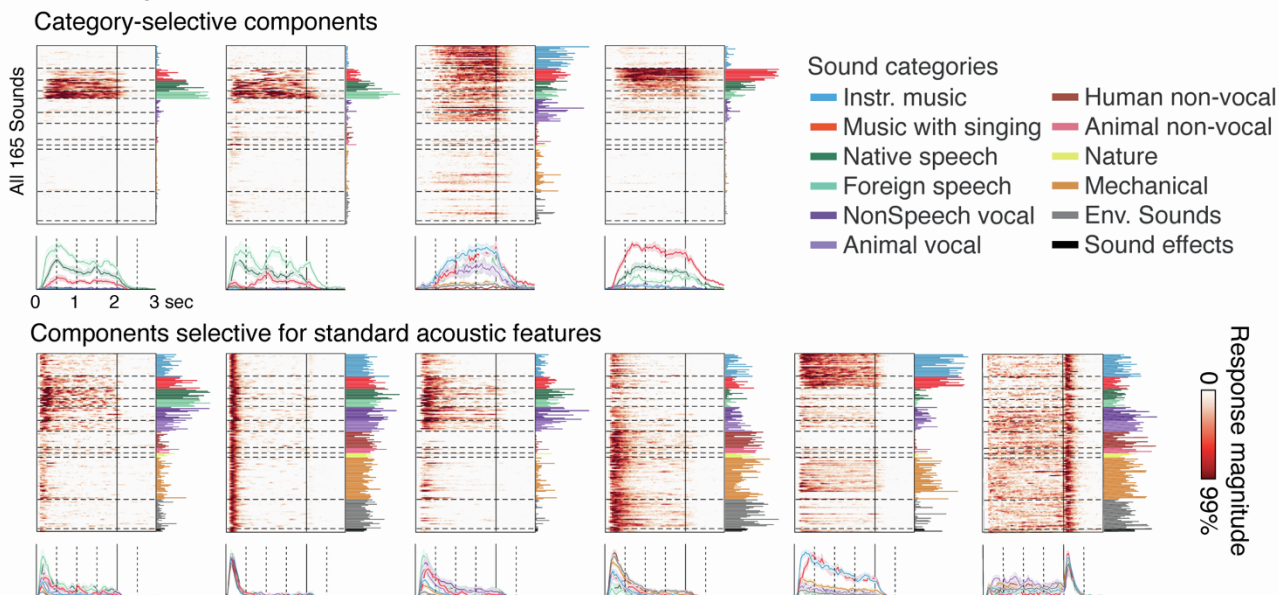


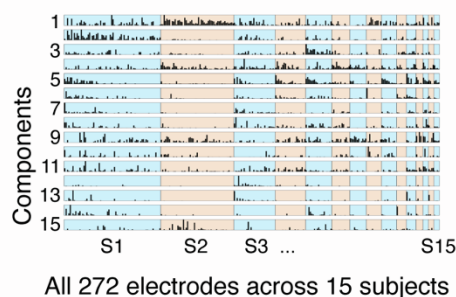
Figure S1. Component model and relevant statistics, Related to Figure 1. A, Histogram of broadband gamma response amplitudes pooled across all timepoints, sounds, and electrodes. Responses were measured relative to the pre-stimulus baseline (300 milliseconds preceding sound onset). The histogram was measured in a cross-validated fashion to reduce the effects of noise (see Methods). Positive responses accounted for >99.9% of the RMS response

power. **B**, The normalized autocorrelation function (normalized by the correlation at zero lag) for all electrodes, measured in a cross-validated fashion by correlating the response in odd and even runs at different lags (gray lines show individual electrodes; black line shows the mean). The extent of temporal dependencies varied substantially across electrodes. **C**, We measured the skew (3rd moment) and sparsity (excess kurtosis) of each electrode's response using its distribution of response magnitudes across all timepoints/stimuli. This figure plots a histogram of the skew and sparsity values across all electrodes. All electrodes were skewed and sparse relative to a Gaussian. **D**, For each sound, we measured the skew and sparsity of responses across electrodes, after averaging the response of each electrode to each sound. This figure plots a histogram of the skew and sparsity values across all sounds. **E**, Schematic of the component model, which was motivated by the statistical properties shown in panels A-D. Each electrode was represented by its response timecourse (broadband gamma) across all sounds (measured relative to silence). This timecourse was modeled as the weighted sum of multiple component timecourses to capture the fact that each electrode is influenced by many neurons and thus might reflect multiple underlying neuronal populations. The component response timecourses were the same across electrodes, but the weights varied to account for different response patterns. Both the component responses and weights were constrained to be positive. To encourage the component response patterns to be sparse and skewed, we modeled each component as the convolution of a set of sparse activations with a smoothing kernel. The smoothing kernel was learned separately for each component to account for variable levels of smoothness in the responses across electrodes. **F**, Average squared correlation (noise-corrected) between measured and model-predicted responses in test data as a function of the number of components and sparsity penalty (Figure 2B shows results for the best sparsity parameter ($\lambda = 0.33$)). **G**, Comparison of the prediction accuracy (average correlation in test data) of our model with several baseline models that did not rely on a convolutional decomposition: (1) non-negative matrix factorization (NMF) where the components and weights were constrained only to be positive; (2) NMF with a sparsity penalty applied directly to the responses and weights (+ L1 Sparse); (3) NMF with an L2 smoothness penalty applied to the derivative (first-order difference) of the component responses (+ L2 Sparse); and (4) NMF with both an L1 sparsity and L2 smoothness penalty (+ L1 & L2). Error bars show the median and central 68 percent of the sampling distribution measured via bootstrapping across subjects.

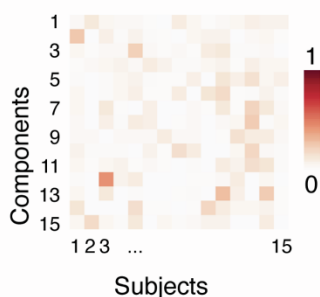
A NMF components



B Component electrode weights



C Average weight per subject



D Less-reliable components

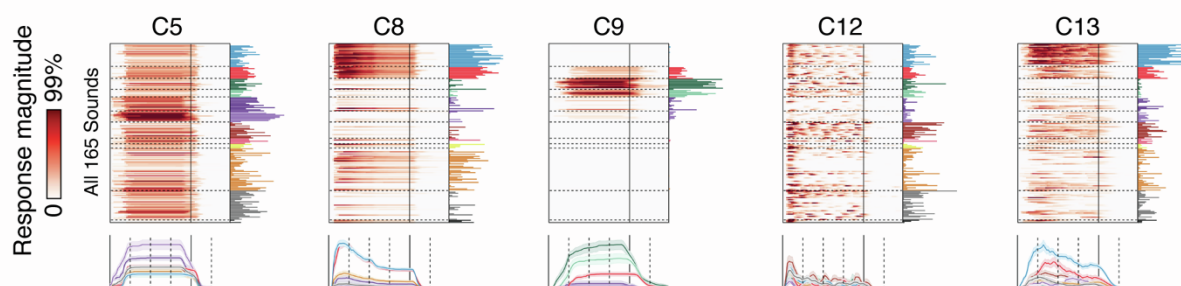


Figure S2. Component reliability, Related to Figures 2 & 5. **A**, The 10 reliable components estimated from our component model were also clearly evident in a simpler model that just imposed non-negativity on the responses and electrode weights (non-negative matrix factorization or NMF). This figure plots those components. As in the main text, the components are grouped into those that responded selectively to speech, music, or song (top, compare with Figure 2A) and those that showed selectivity for standard acoustic features (bottom, compare with Figure 5A). **B**, The distribution of weights across all electrodes for each component. Electrodes from different subjects have been grouped together, and the subjects have been ordered based on the total number of sound-responsive electrodes in their dataset. **C**, The average weight of each component in each subject, normalized so that the weights across subjects sum to 1. As a consequence, large values indicate that a component primarily explained responses from a single subject. Most components had weights that were distributed across a large number of electrodes from several different subjects. Component 12 weighted strongly on a single subject (S3) and was not included in the figures in the main text for this reason. **D**, This figure shows the response of components that were less reliable than those plotted in the main text, either because they differed from those present in a simpler NMF model (C5, C8, C9, C13) or weighted heavily on a single subject (C12).

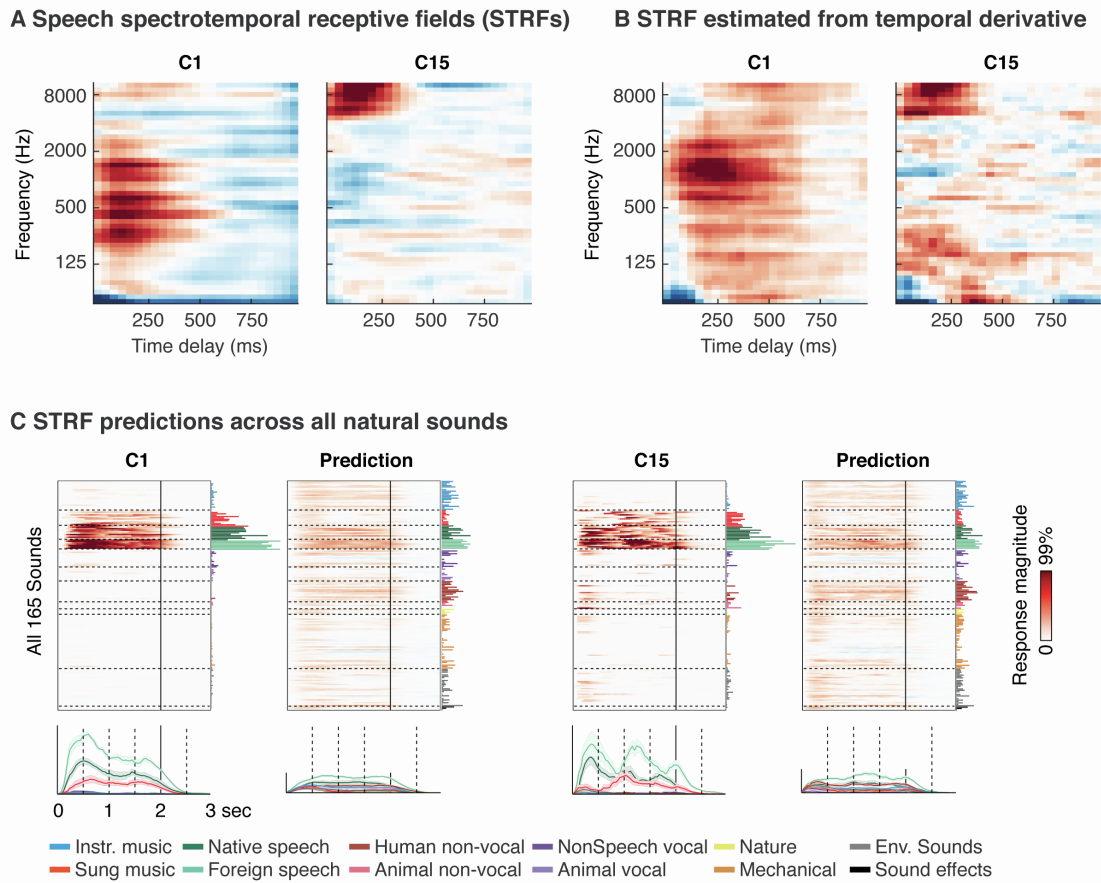


Figure S3. Spectrotemporal receptive field (STRF) analysis for speech-selective components, Related to Figure 2. **A**, Spectrotemporal receptive fields, measured by estimating a linear mapping between a cochleagram representation of sound and the responses of the speech-selective components (C1, C15) (ridge regression with 5-fold cross-validation). The STRF was estimated from the components' response to speech (English and foreign speech). **B**, The half-wave rectified temporal derivative (difference between adjacent samples) was included in the regression analysis, which we found improved performance. This panel plots weights for the temporal derivative features as a time-frequency plot. The weights in panels a and b were computed from a single model with both sets of features. **C**, Predictions from a STRF model trained on all 165 natural sounds. The target and predicted response for the two speech-selective components are shown side by side (format is the same as Figure 2A). STRFs fail to capture the clear speech-selectivity evident in the component responses.

Prediction of ECoG song-selective component from fMRI

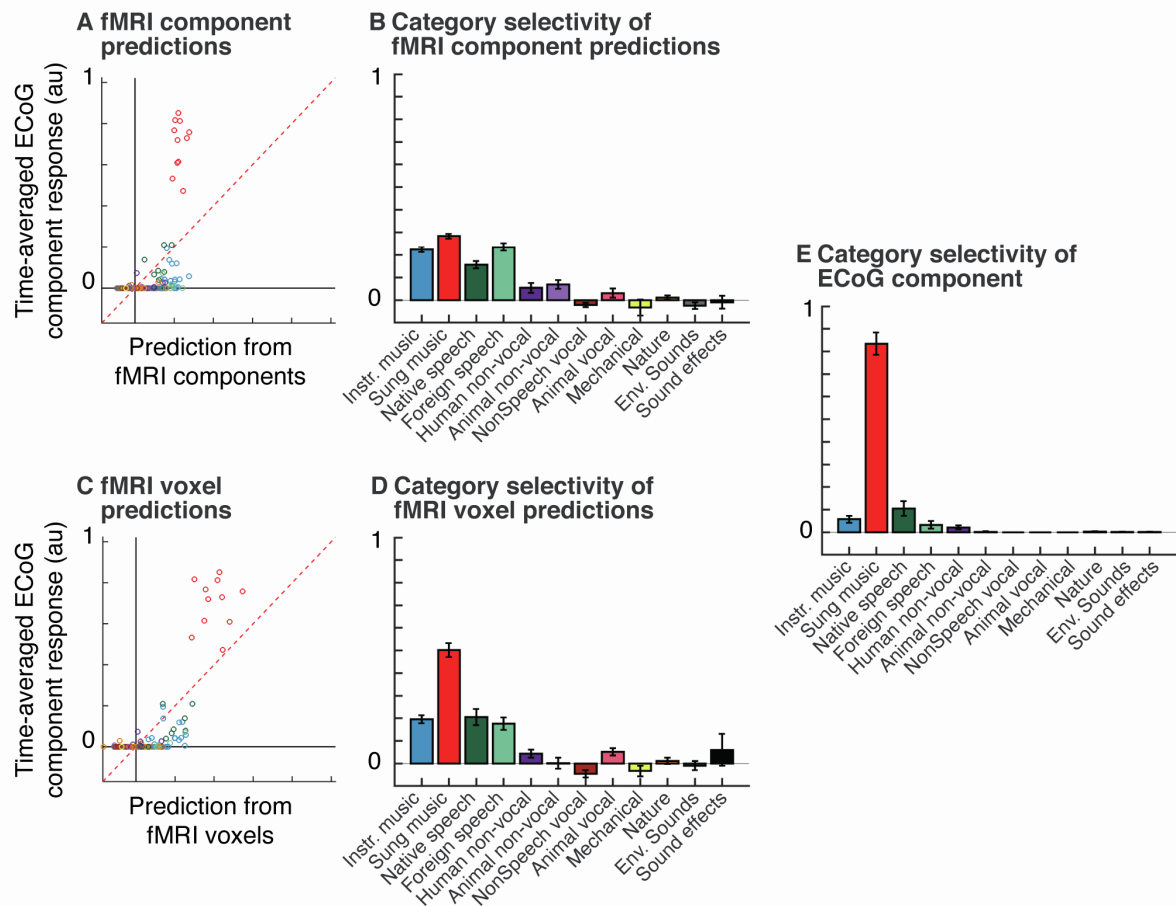
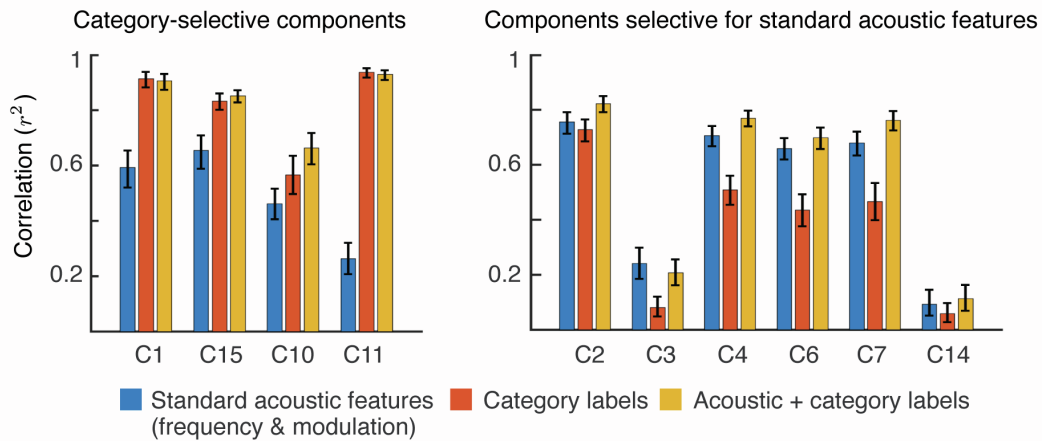


Figure S4. Attempting to predict song selectivity from fMRI responses, Related to Figures 2 & 7. **A**, We previously inferred a set of fMRI components that showed selectivity for speech and music, individually. To test whether the song-selective component (C11) could be explained as a weighted sum of speech and music selectivity (or any other fMRI component), we regressed the fMRI components against the time-averaged response of the song-selective component (using ridge regression with five-fold, nested cross-validation across the sound set). This panel plots a scatter plot of the predictions. **B**, Average response of the fMRI component predictions to different categories, revealing the absence of song-selectivity. **C-D**, We also attempted to predict the song-selective ECoG component using the original voxel responses to test if there was any additional song selectivity present in the voxels that was not present in the components. Same format as panels A-B. The fMRI voxel predictions showed greater song selectivity than the fMRI component predictions but were less song-selective than the ECoG component. **E**, For reference with panels B and D, here we plot the average response of the song-selective ECoG component to different categories.

A Prediction accuracy



B Prediction of song-selective component from standard acoustic features

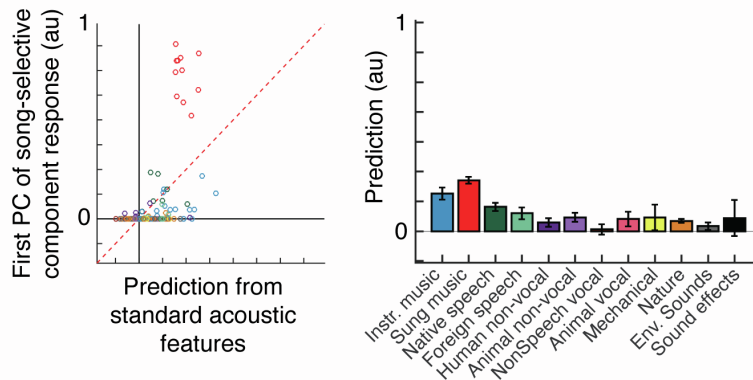


Figure S5. Acoustic prediction analyses, Related to Figures 2, 4, and 5. A, We attempted to predict the response of each component as a linear function of standard acoustic features (based on frequency and modulation tuning), category labels, or both standard acoustic features and category labels. As in our other acoustic analyses (**Figure 5D&E**), the response of each component was summarized by the first PC of the sound x time response matrix, which accounted for the dominant response variation across stimuli. This figure plots the squared Pearson correlation between the cross-stimulus variation in the first PC and the prediction of that variation from the three feature sets. The left plots show the four category-selective components whose anatomical weights were more concentrated in non-primary regions. The right plots show the more primary-like components, whose response appeared to correlate with standard acoustic features. As expected, category labels explained more variance in the category-selective components, with little additional variance explained by the frequency and modulation features, while the acoustic features explained more variance in the more primary/acoustically selective components. **B,** The best-fitting acoustic predictions for the song-selective component (C11). The left panel shows a scatter of the predictions, and the right panel shows the predictions averaged within categories, which demonstrates the absence of clear song selectivity.

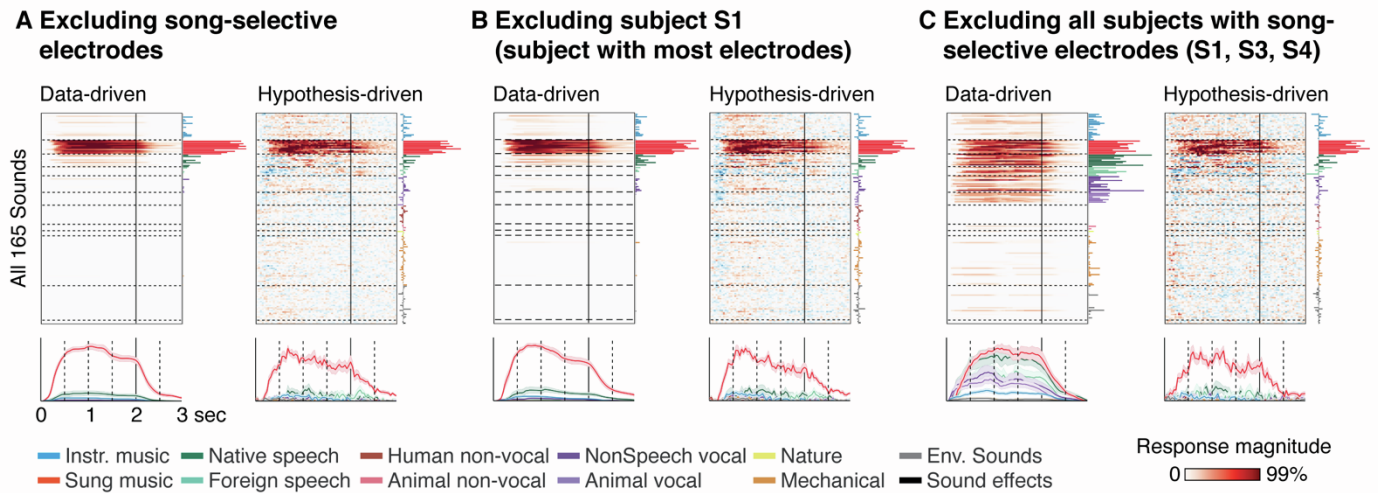
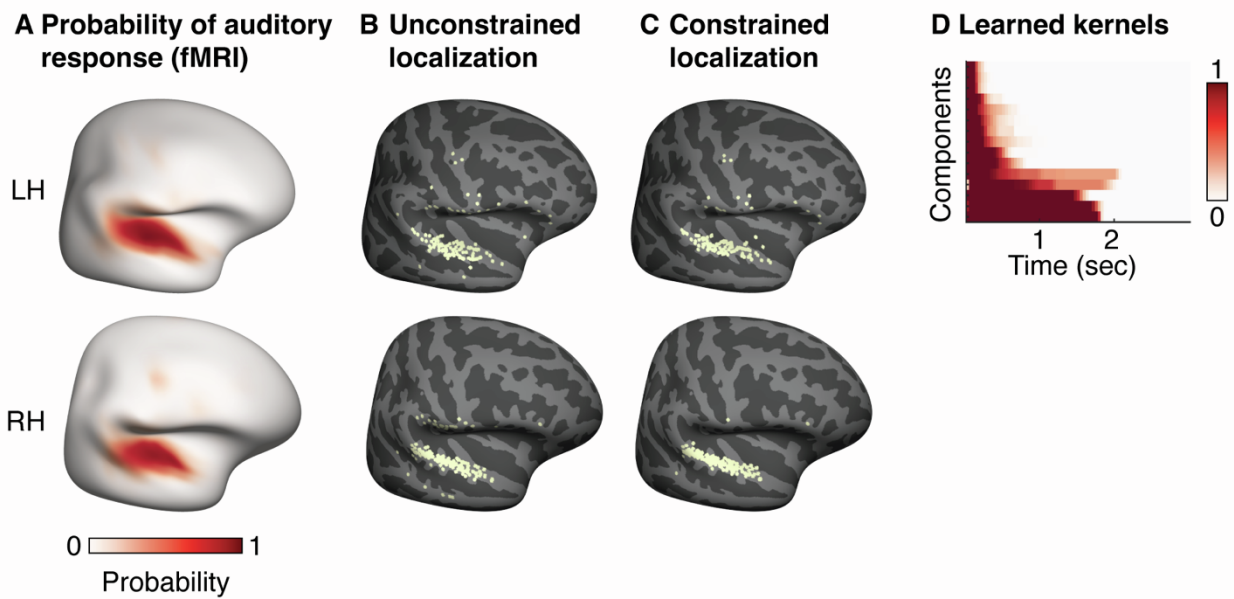


Figure S6. Effect of excluding electrodes and subjects, Related to Figures 2 and 3. **A**, Song-selective components inferred after excluding all song-selective electrodes (shown in Figure 6). Results are shown using both our data-driven (left, compare with Figure 2A) and hypothesis-driven (right, compare with Figure 3) analysis methods. Note that two song-selective electrodes were already discarded from our original analysis because their test-retest reliability fell below our cutoff ($r > 0.2$). **B**, We repeated our component analyses 15 times, each time excluding all of the electrodes from one subject. Both the hypothesis and data-driven methods revealed a clear song-selective component in every case. This panel plots the song-selective component inferred after excluding all of the electrodes from S1, who had the most electrodes of any subject (70 electrodes out 272 total) including several song- and music-selective electrodes. **C**, We repeated our component analyses excluding electrodes from all of the subjects with song-selective electrodes (S1, S3, S4). We did not observe a song-selective component using the data-driven method: the left panel plots the component whose response correlated best with the song-selective component inferred from the entire dataset, which was not selective for singing. However, we did observe a clear song-selective component using the hypothesis-driven method, demonstrating that song selectivity is present in the other subjects but harder to detect using statistical criteria alone.



E Operations used to enforce unimodality of kernel

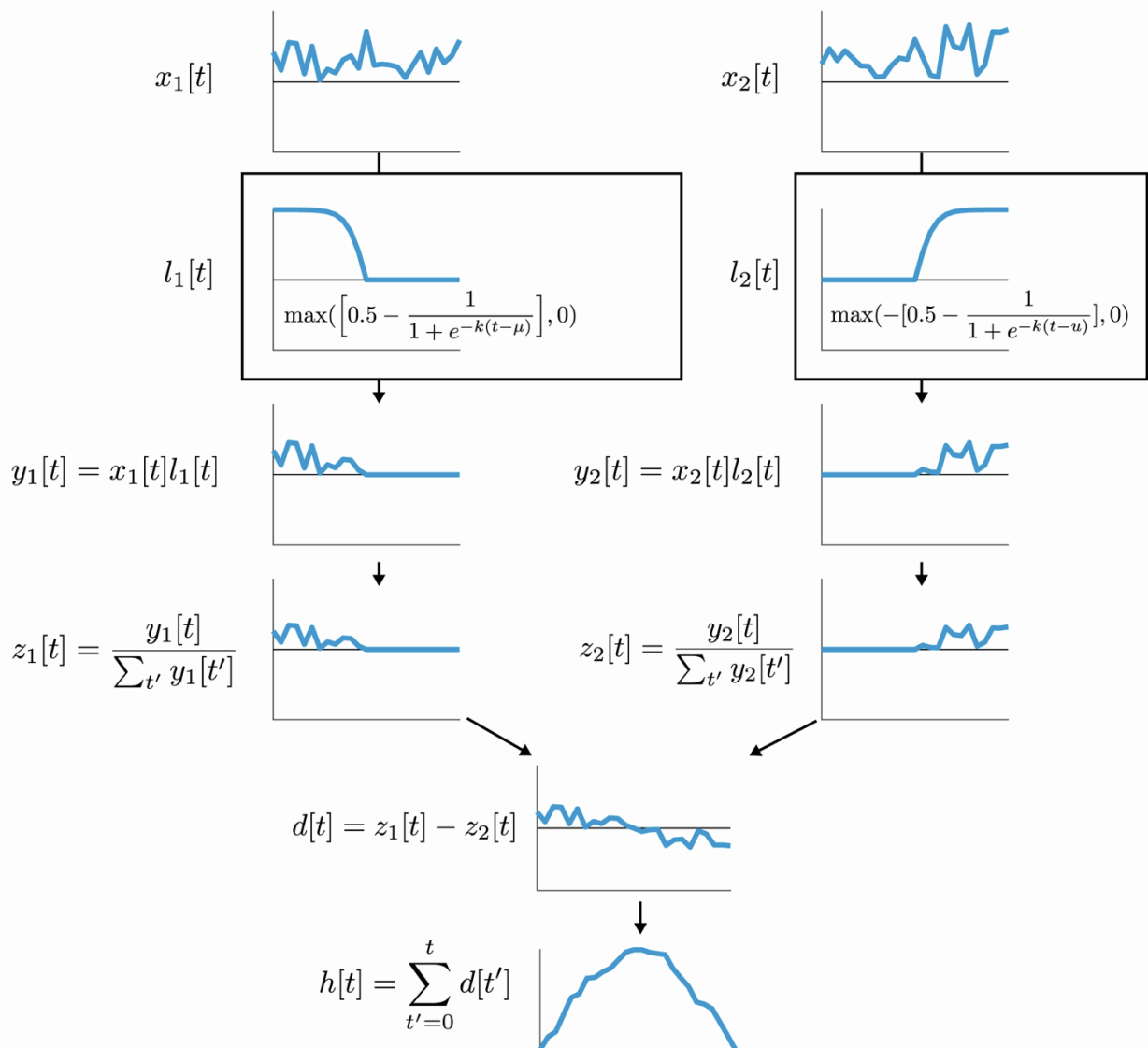


Figure S7. Methods details, Related to Figures 1, 2, & 5. **A**, Map showing the probability of observing a significant response to sound at each point in the brain. The map was computed using fMRI responses to the same sound set in a large cohort of 20 subjects with whole-brain coverage. **B**, Electrode localization without correction. Small errors in localization likely explain why some electrodes have been localized to the middle temporal gyrus and

supramarginal/inferior frontal gyrus, which abut the superior temporal gyrus where responses to sound are much more common. **C**, To minimize gross localization errors, we treated the probability map of sound-driven responses shown in panel A as a prior and used to it constrain the localization (see *Electrode localization* in the Methods). Our approach did not substantially affect the localization of electrodes at a fine scale but minimized gross errors by for example encouraging electrodes to be mapped to the superior temporal gyrus rather than the middle temporal if they were nearby to both. **D**, This figure plots the learned smoothing kernels as a raster, with each row corresponding to a different kernel. The kernels have been sorted by the first principal component of the matrix. The kernels vary widely in their extent/duration. Many of the kernels were also asymmetric with a fast/instantaneous rise and a slower falloff. **E**, This plot describes the set of operations (implemented in TensorFlow) that was used to constrain the smoothing kernel to be unimodal. Conceptually, the goal of these operations is to force the derivative to be exclusively positive for the first N time-points and then exclusively negative for the rest of the signal, thus preventing oscillations. We also must force the sum of the derivative to equal zero so that the kernel starts and ends at zero. Two positive vectors (themselves computed as the absolute value of real-valued vectors) were multiplied by rectified logistic functions that had the effect of zeroing out the beginning or end of the signal. The two vectors were then normalized so that they sum to 1, subtracted, and cumulatively summed, yielding a unimodal signal. The shape of the kernel is determined by the values of the two input vectors (x_1 and x_2) as well as the parameters of the logistic function (μ and k), all of which were learned. The input vectors were initialized with a vector of ones, μ was initialized to the value of the middle time-point, and k was initialized to the value of 1 (and prevented from taking a value less than 0.001).